Differential Bandgap Solar Cell Analysis

Thesis by

Alexander Patrick McCormick Place

In Partial Fulfillment of the Requirements for the degree of

Bachelor of Science

California Institute of Technology

Pasadena, California

2017

(Submitted May 15, 2017)

Acknowledgements

I am deeply grateful to Professor Julia Greer for providing me with an opportunity to pursue my passion. I am also indebted to the members of her group, especially Akira Kudo for mentoring me throughout my thesis. Andrey Vyatskikh, Ryan Ng, Amanda Bouman, and Arturo Mateos all provided significant help as well.

I am also forever grateful to my true family as well as all of my friends here at Caltech, who truly feel like family.

1 Abstract

This thesis proposes and analyzes a new solar cell design. The base electrode of the new photovoltaic is composed of several electrically isolated nanolattices suspended on top of each other. Doped semiconductors are then deposited onto the beams of this electrode, forming isolated p-n junctions. The deposition thicknesses of one of the doped semiconductors is varied along the height of the device, creating a multi-junction solar cell. The charge carrier dynamics in an amorphous silicon- and germanium-based device are simulated, and the efficiency is found to be a factor of four greater than a conventional planar structure with similar parameters. The main components of this photovoltaic's fabrication process are developed and analyzed. Specifically, suspended and electrically isolated lattice electrodes made of carbon are built. The electrical conductivity of the carbon is shown to be similar to that of indium-tin oxide. The electrode material is determined to be a mix of amorphous and glassy carbon. Different methods of radio-frequency sputter deposition are used to deposit spatially dependent layer thicknesses of semiconductors onto the lattice beams. The spatial dependence is shown to be approximately linearly dependent on the height dimension of the lattice.

Table of Contents

2 Introduction

2.1 Motivation

Even though the energy from the sun that arrives at the surface of the Earth in one hour is greater than the total energy humans consume in a year (1), as of 2015 less than 1% of the energy produced in America is done so through solar power (2). In order to increase the number of photovoltaic (PV) cells employed, and likewise decrease our energy sector's harsh impact on the environment, several problems need to be addressed. This thesis explores a device that significantly fixes two of the main hurdles: low efficiencies and high footprints of PV cells.

2.2 Basics of Photovoltaics

In a simplified model, a single-junction solar cell (the most popular device geometry as of 2017) can be thought of as two semiconductors stacked on top of each other. One of these semiconductors is doped with acceptor impurities (called the p-type material) while the other is doped with donor impurities (the n-type material). The difference in dopants causes an electric field to form in-between the two regions. When the sun shines on the cell, incident photons are "absorbed"; photons interact with an electron, moving the electron from the valence to the conduction band in the semiconductor via the photoelectric effect. Drift force due to the electric field along with diffusive forces due to the inhomogeneous doping then cause the excited electrons to move towards the n-type side (and the holes towards the p-type side), creating a current pointing towards the p-type side. It is this current that then powers the load attached to the solar cell.

2.2.1 P-N Junctions

Many of the physical phenomena that arise in solar cells have to do with the simpler case of a p-n junction. I will briefly review several of the most relevant aspects of the physical processes in these junctions. This analysis is aided by (3, 4), which are also good references for a more general review of p-n junctions.

A p-n junction, like a photovoltaic, is composed of a p-type semiconductor attached to an n-type semiconductor (Figure 1). When these two types of semiconductors come into contact, the majority charge carriers of both sides will start to diffuse into the other sides. During this diffusion, mobile charge carriers combine with carriers of the opposite polarity, depleting part of the volume where diffusion occurred of any mobile charge carriers[1]—this region is called the depletion region. The depletion region is charged due to ionized nuclei left behind, creating an electric field against the diffusion of the majority charge carriers. Equilibrium is achieved when the diffusion of majority charge carriers and the counteracting force from the electric field in the depletion region are balanced.

---

[1] Of course, mobile charge carriers can enter this region, at which point the charge carriers either have enough energy to overcome the potential drop across the depletion region and therefore will travel through and out of the region, or the charge carriers will be forced back towards where they came from by the electric field. At the end of both scenarios the depletion region is left without mobile charge carriers.

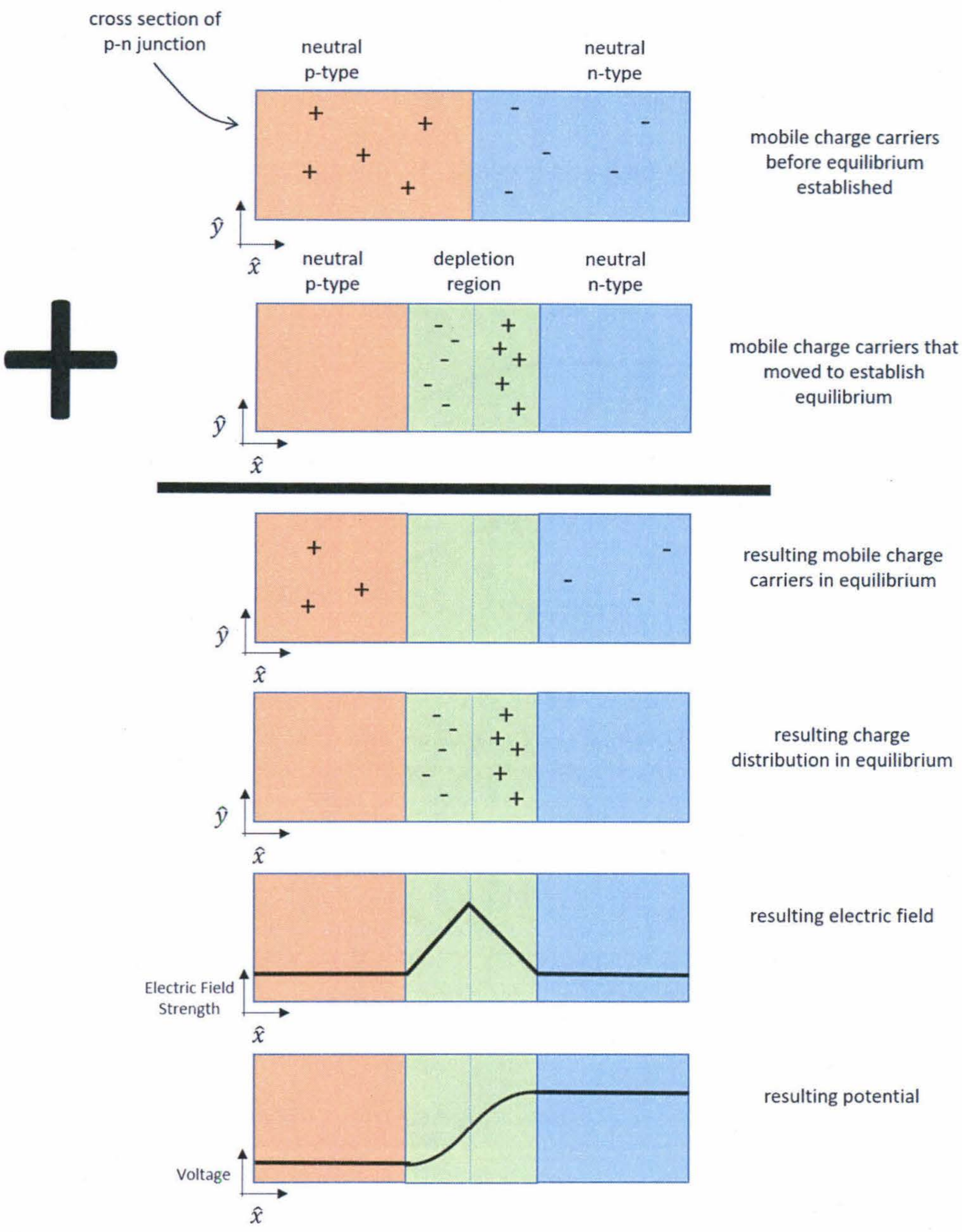

Figure 1: Overview of P-N Junctions

There are two competing currents that pass through the depletion region. First, any minority carrier that is thermally generated in the depletion region, or close enough to wander into the region before recombining, will experience a force due to the electric field. Holes will be forced towards the p-side, while electrons will be forced towards the n-side, so the movement of these two charge carriers create a current in the same direction (Figure 2). The net current due to thermal generation is called the *generation current*, J_{gen}.

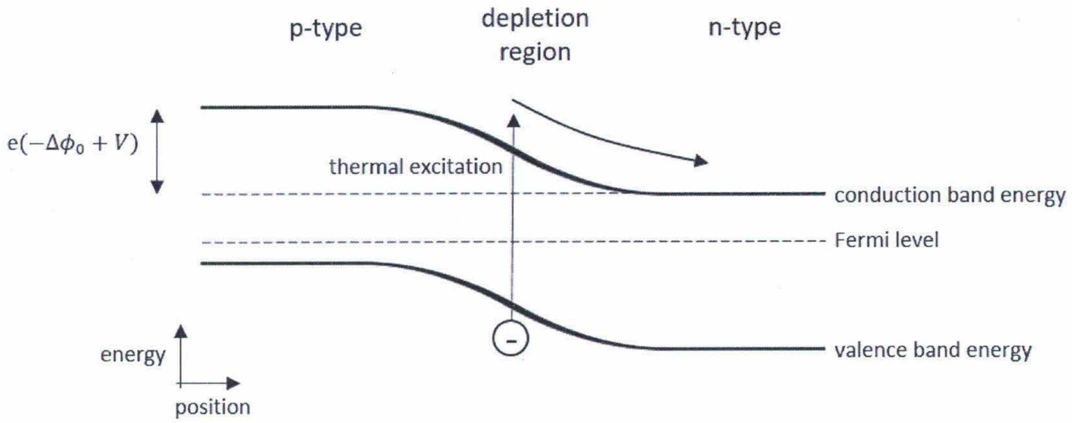

Figure 2: Band Diagram and Generation Current Overview
The two curved band energy plots give the energy of an electron, whose charge is denoted by e in the plot, at the respective band edge as a function of the position of the electron on a line that runs from the p-type material, through the depletion region, and into the n-type material. The generation current is caused by electrons being excited through thermal fluctuations into the conduction band. In the conduction band the electrons, on average, move towards the lowest energy position. Accordingly, the electrons flow towards the n-type material, creating a current.

A competing current arises from charge carriers which have enough kinetic energy to be able to cross the depletion region in the direction opposite of the force applied on the carriers by the electric field. Once majority carriers travel across the depletion region they become minority carriers, and will likely recombine. Accordingly, the current that arises from this phenomenon is called the recombination current, J_{rec}. Assuming that the energy of the carriers follows a Boltzmann distribution (see (3), for example), the number of charge carriers with sufficient energy to cross the voltage barrier, and therefore the resulting current, has the relation:

$$J_{rec} = \alpha e^{\frac{-\Delta\phi_0+V}{kT}}, \tag{1}$$

where V is the external voltage applied across either end of the junction (where a positive voltage is defined to mean that the p-side is at a higher potential than the n-side), $\Delta\phi_0$ is the voltage difference across the depletion region when $V = 0$, and kT is Boltzmann's constant multiplied by the temperature.

In order to clarify the meaning of the proportionality constant α, consider a situation where the ends of the diode are attached to each other without a load, making $V = 0$. No net current could flow because no power is being input into the system[2]. Accordingly the two currents must balance each other out:

$$(\alpha e^{\frac{-\Delta\phi_0+V}{kT}} + J_{gen})|_{V=0} = 0 \tag{2}$$

which shows

$$\alpha e^{\frac{-\Delta\phi_0}{kT}} = -J_{gen} \tag{3}$$

This result could have been predicted: an increase in the number or electrons that are excited to the conduction band is indicative of a larger tale on the high-energy end of the

---

[2] If a net current could flow in the junction's equilibrium state, then we'd have a nonzero potential and current which would flow through the resistive semiconductor material. This would dissipate energy even though no energy is being input into the system, violating the principle of conservation of energy.

probability of occupancy function. This larger tale also means more mobile charge carriers will have enough kinetic energy to surpass the potential barrier to cross the depletion region.

Summing the currents in a p-n junction for any V gives:

$$I_{p-n} = J_{gen}(e^{\frac{V}{kT}} - 1) \qquad 4$$

Now the only unknown quantity in I_{p-n} is J_{gen}. To find an expression for J_{gen}, first consider the number of charge carriers in the device. We know that the number of electrons in the conduction band per unit volume, n, is simply an integral of the density of states multiplied by the Fermi distribution function:

$$n(x) = \int_{\epsilon_c}^{\infty} N(\epsilon) \frac{1}{e^{\frac{\epsilon - \mu_n(x)}{kT}} + 1} d\epsilon \qquad 5$$

where ϵ_c is the lowest possible energy of an electron in the conduction band, $N(\epsilon)$ is the density of states, $\mu_n(x)$ is the quasi-Fermi level (also called “imref”, which is “fermi” backwards) of the conduction band[3] at position x along the device, and e is the charge of an electron. Assuming $\epsilon - \mu(x) \gg kT$, n simplifies to

---

[3] Note that μ_n is the quasi fermi level *for the conduction band*. When the material is in equilibrium, the conduction and valence quasi-Fermi levels are the same. However, when the system is not in equilibrium—for example, when an electron excited by a photon resides in the conduction band—the equilibrium Fermi level doesn’t accurately model the system: there are an increased number of both electrons in the conduction band and holes in the valence band relative to the equilibrium state before the electron was excited by a photon. Instead, both bands can be thought of as having independent quasi-Fermi levels, the Fermi level that leads to the given state of the charge carriers in the respective band.

$$n(x) \approx \int_{\epsilon_c}^{\infty} N(\epsilon) e^{\frac{-(\epsilon-\mu_n(x))}{kT}} d\epsilon = e^{\frac{\mu_n(x)-\epsilon_c}{kT}} \int_{\epsilon_c}^{\infty} N(\epsilon) e^{\frac{-(\epsilon-\epsilon_c)}{kT}} d\epsilon \equiv N_c e^{\frac{\mu_n(x)-\epsilon_c}{kT}} \qquad 6$$

and likewise the density of holes, p, is:

$$p(x) = \int_{0}^{\epsilon_v} N(\epsilon) \frac{1}{e^{\frac{\mu_p(x)-\epsilon}{kT}}+1} d\epsilon \approx \int_{0}^{\epsilon_v} N(\epsilon) e^{\frac{(\epsilon-\mu_p(x))}{kT}} d\epsilon \qquad 7$$

$$= e^{\frac{\epsilon_v-\mu_p(x)}{kT}} \int_{0}^{\epsilon_v} N(\epsilon) e^{\frac{(\epsilon-\epsilon_v)}{kT}} d\epsilon \equiv P_v e^{\frac{\epsilon_v-\mu_p(x)}{kT}}$$

Notice that when the device is in equilibrium, as the Fermi level changes the number of electrons in the conduction band increases by the same factor as the number of holes in the conduction band decreases: $e^{\frac{\mu(x)}{kT}}$. This asymmetric behavior leads to a conserved quantity, independent of μ:

$$np = N_c P_v e^{\frac{\epsilon_v-\epsilon_c}{kT}} = N_c P_v e^{\frac{-\mathrm{E_g}}{kT}} \qquad 8$$

where $E_g = \epsilon_c - \epsilon_v$ is the bandgap of the semiconductor. Accordingly, np is a measure of the number of mobile charge carriers—electrons in the conduction band and holes in the valence band. To this end, the density of intrinsic carriers in a semiconductor—the number of mobile charge carriers—is defined as $n_i^2 \equiv np|_{V=0} = N_c P_v e^{\frac{-\mathrm{E_g}}{kT}}$.

With the definition of n_i in mind, consider the process of thermally exciting an electron from the conduction to the valence band. This process is dependent on the number of electrons in the valence band which have enough energy to surmount the bandgap of the semiconductor. Thus the rate of thermal excitation of electrons into the conduction band should be dependent on the number of charge carriers in the valence band and independent of the number of charge carriers in the conduction band[4]. One such quantity is $n_0 \equiv \frac{n_i^2}{p}$. Accordingly, the electron lifetime τ_n is defined such that:

$$\frac{rate\ of\ thermal\ excitation\ of\ electrons}{volume} = \frac{n_0}{\tau_p} \qquad 9$$

And likewise for the valence band:

$$\frac{rate\ of\ thermal\ excitation\ of\ holes}{volume} = \frac{p_0}{\tau_p} \qquad 10$$

Circling back to the original point of this discussion, intuitively we can expect that any charge carrier created in or near the depletion region will contribute to J_{gen}. In this case, (3) shows that "near" means within approximately half of a diffusion length. Therefore, the number of holes thermally excited in an area which will travel across the depletion region in a unit of time is given by

$$J_{gen,holes} = \frac{\boldsymbol{rate\ of\ valence\ band\ hole\ thermal\ generation}}{\boldsymbol{volume}} * L_p = \frac{p_0}{\tau_p} L_p \qquad 11$$

with a similar result for electrons[5]. Accordingly,

---

[4] This discussion assumes that the electron levels near the bottom of the conduction band aren't full.

[5] This is neglecting the carriers generated within the depletion region because the argument assumes that the depletion region is small. This is not a good assumption for many solar cells, as will be discussed later.

$$I_{p-n} = \left(\frac{p_0}{\tau_p}L_p + \frac{n_0}{\tau_n}L_n\right)(e^{\frac{V}{kT}} - 1) \qquad \mathbf{12}$$

2.2.2 Photovoltaics

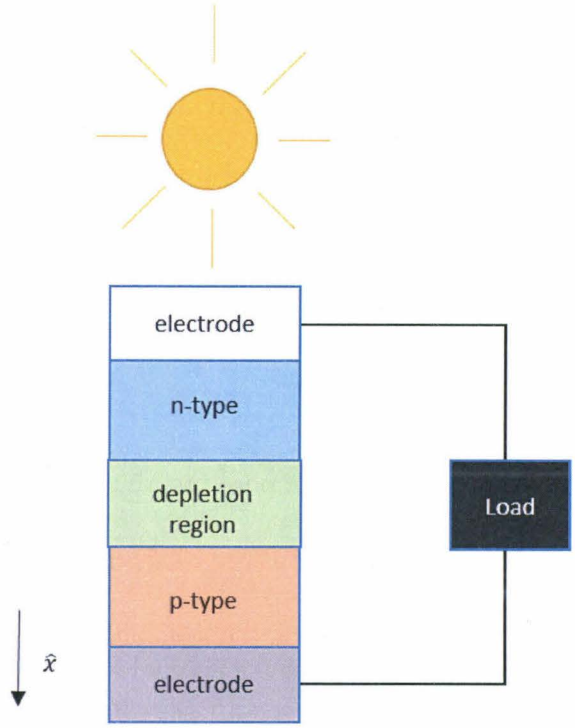

Figure 3: Single Junction Photovoltaic Device Overview

A single-junction photovoltaic likewise has a p-n junction and the accompanying recombination and generation currents discussed above. The main difference, however, is the current created by the photoexcitation of carriers, I_L. This new current can be thought of as an addition to the thermal generation current—electron-hole pairs created by either light or thermal excitations behave in the same way after being generated. Therefore, the current in the device becomes:

$$I_{PV} = \left(\frac{p_0}{\tau_p}L_p + \frac{n_0}{\tau_n}L_n\right)\left(e^{\frac{V}{kT}} - 1\right) - I_L \qquad \mathbf{13}$$

The next question is: how is I_L determined? I_L depends on the number of electron-hole pairs excited by incident light[6] in a region where, once separated, at least one of the carriers is influenced by a drift or diffusive force to move—in other words, I_L is given by the number of electron-hole pairs excited in and within a diffusion length of the depletion region. The number of electron-hole pairs generated in this region from the incident spectrum of the sun, $\phi(\omega)$, is dependent on the material under consideration. Specifically, the probability that a particular frequency of light will be absorbed after travelling a unit distance in the material, which is measured by the absorption coefficient $\alpha(\omega)$, is important. The details of this will be worked out below, though intuitively the number of photons which excite electrons is dependent on 1) how well the semiconductor material absorbs the wavelengths of light incident from the sun and 2) the volume where excited electrons and holes add to I_L—the volume of the depletion region and material less than one diffusion length away from the depletion region.

---

[6] For indirect bandgap photovoltaics, which include Si, phonons are also involved in exciting electron-hole pairs.

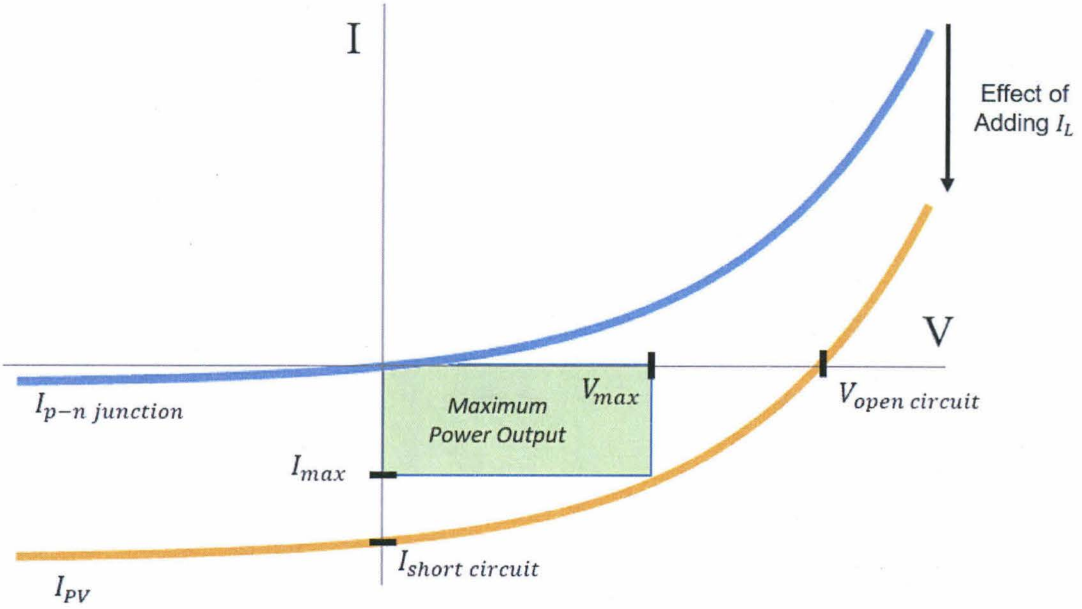

Figure 4: Current vs. Voltage Characteristics of P-N Junctions and Photovoltaics
The area of the box with edge lengths I_{max} and V_{max} give the maximum power output by the photovoltaic.

The power generated by a solar cell is a product of both the current and the voltage output by the device. The recombination current causes an exponential relationship between the current and voltage, demonstrated in Figure 4. Accordingly, the maximum current is attained when the device is short circuited, and the maximum voltage is produced when no current flows through the device. The power is maximized, however, at some $V_{max} < V_{open\ circuit}$ and $I_{max} < I_{short\ circuit}$, as presented in the green square in Figure 4.

To intuitively examine the multiple device parameters which affect the voltage across the device, consider the open circuit voltage V_{oc} by plugging $I_{PV} = 0$ into equation 13:

$$I_{PV}|_{open\ circuit} = 0 = \left(\frac{p_0}{\tau_p}L_p + \frac{n_0}{\tau_n}L_n\right)\left(e^{\frac{V_{OC}}{kT}} - 1\right) - I_L \qquad \textbf{14}$$

which leads to:

$$V_{OC} = kT \ln\left(\frac{I_L}{\left(\frac{p_0}{\tau_p}L_p + \frac{n_0}{\tau_n}L_n\right)} + 1\right) \tag{15}$$

Accordingly, V_{OC} is highly dependent on I_L, which serves to shift the entire I-V curve downwards (Figure 4). E_g is another factor that affects V_{OC}. Since p_0 and n_0 are both proportional to $n_i^2 \propto e^{\frac{-E_g}{kT}}$, V_{OC} increases with E_g. I_L is also dependent on E_g, as E_g sets the lower bound for the energies absorbed by the solar cell. However, at room temperature, $kT \approx 26\ meV$, which is a small fraction of the bandwidth of the sun's spectrum: a change in E_g by $26\ meV$ will alter n_i^2 by a factor of e while it will have only a negligible effect on the number of photons absorbed, and subsequently I_L.

2.3 Review and Analysis of Solar Cell Designs

With the basic equations modeling solar cells in hand, the next question is: which parameters in these equations do different solar cell designs exploit to maximize efficiency? I'll explore and analyze several of the most common and relevant designs: single junction, multi-junction, and nanowire solar cells.

2.3.1 Single Junction Solar Cells

In its most basic form, a single junction solar cell has the same geometry as described in the analysis above (Figure 3): two planes of semiconductors stacked on top of each other. One plane is doped with acceptors (the p-type region), the other is doped with donors (the n-type region). A depletion region forms between the two planes. As discussed above, I_L is dependent on the size of the depletion region—to increase the photocurrent, many solar cells will include a third, intrinsic region in-between the two doped regions, creating a p-i-n junction. When the depletion region in this junction is being formed, electrons are forced by a diffusive force to enter the intrinsic region. There the electrons need to diffuse a longer distance until they find a hole to recombine with, since the intrinsic region is without dopants. Accordingly, the depletion region is extended.

However, increasing the length of the depletion region leads to a significant drawback: the further that a charge carrier has to move to reach an electrode, the higher the likelihood of the charge carrier recombining with the opposite charge—dissipating the energy which was used to excite the charge carrier. For example, an electron that is excited on the p-type edge of the depletion region has to move across the intrinsic layer in addition to the n-type layer. In an ideal case the depletion layer has no holes, though in actuality it will be filled with material defects which lead to recombination.

There is a second significant tradeoff in single junction solar cells: the magnitude of the voltage across the device increases with E_g as demonstrated by equation 15, while the current has a complex dependence on E_g as shown in equation 13.[7] Accordingly, there is an ideal bandgap to maximize the power output of the cell: 1.35 eV (5).

---

[7] See the discussion of the E_g dependence in equation 15 to better understand the E_g dependence in equation 13.

As mentioned above, as E_g increases I_L decreases. This is because only photons with energy equal to or above the bandgap are able to excite an electron to the conduction band. Therefore, for a single junction solar cell, low energy photons can no longer excite electrons to the conduction band if E_g is too large; in other words, an increase in E_g reduces the amount of the sun's spectrum which a device can convert to electricity. Due to this constraint, optimized single junction solar cells are limited to have low bandgaps. Hence, any photon with energy above these low bandgaps has part of its energy wasted. The energy above the bandgap isn't collected because the excited electron settles to near the conduction band edge, only approximately a bandgap above the energy which the electron had before interacting with the photon. Single junction solar cells, therefore, have to compromise voltage in order to be able to collect a larger frequency range of the solar spectrum. As explained in the next section, multi-junction solar cells are an alternative which have been developed to significantly mitigate this problem.

2.3.2 Multi-junction Solar Cells

With single-junction photovoltaics, the tradeoff between absorbing photons at low energies and exploiting high energy photons restricts the maximum efficiency[8] to 31% for a standard air mass 1.5 terrestrial spectrum (5). However, the effects of this tradeoff can be mitigated if the flux of photons with a range of energies is collected at different voltages—we can stack several junctions in a device, creating a multi-junction solar cell (Figure 5). Consider a

---

[8] Specifically, power conversion efficiency: the output power of the cell divided by the incident power from the sun on the device.

device with the highest bandgap junction placed on top, and each subsequent junction has a lower bandgap than the previous junction. The photons with the highest energy will be absorbed in the first junction, while the photons with lower energies will propagate to the next junctions. This process will repeat, so that each incident photon will be absorbed by the bandgap which has an energy that is closest to, while still below, the photon's energy. As a result, each incident photon will excite an electron by an amount of energy which is, on average, significantly closer to the energy of the incident photon than the corresponding excited electron if the same photon were to hit a single-junction solar cell. Likewise, the top junctions—the high bandgap junctions—will have significantly higher voltages.

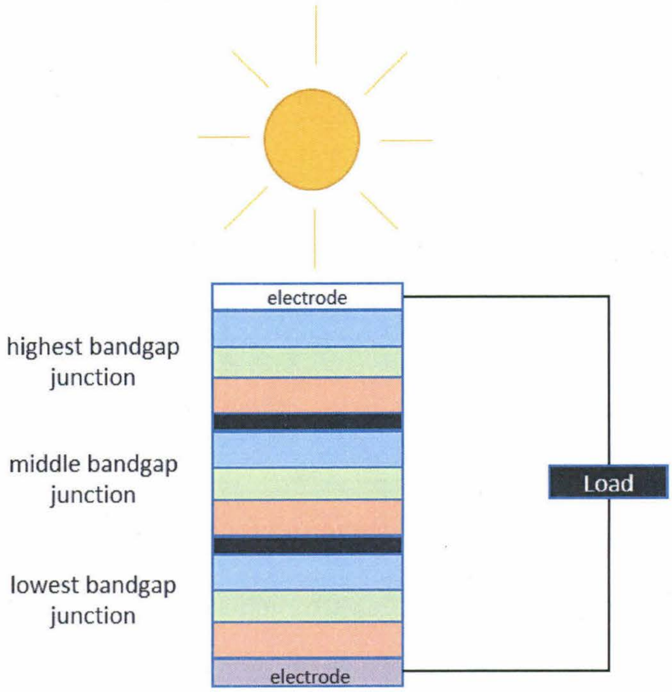

Figure 5: Overview of Multi-junction Photovoltaic

Consider a single-junction (SJ) solar cell and a multi-junction (MJ) solar cell whose lowest bandgap is the same as the SJ device, with each device having comparable depletion region volume[9]. Each junction in the MJ cell will absorb a portion of incident photons, and the whole device will absorb the equal number of photons as the SJ cell would. Nevertheless, increased power output is typically acquired by the MJ cell since photons absorbed in the top junctions will produce a higher voltage than they would in the SJ cell.

An ideal multi-junction solar cell is "lattice-matched", or made out of materials that have the same lattice constant, so that there is a smooth transition without defects, which cause recombination, between the junctions. Further, the junctions in a typical multi-junction solar cell are in series—requiring all of the junctions to have the same current. This means that an ideal cell will be "current-matched" so that J_{max} for each of the junctions is the same.

2.3.3 Nanowire Solar Cells

Another problem with a typical SJ solar cell is a large excitation-electrode distance, which deteriorates the energy output. As discussed above, ideally the depletion region is large enough and the absorption characteristics of the semiconductor good enough so that all of the incident photons excite electrons in the cell. However, this often requires significant depletion region volumes which increases the average excitation-electrode distance—the distance of the path an electron takes from the point where the charge carrier was excited to the electrode

---

[9] By "comparable depletion region volume" I mean that the net volume of all of the junctions in the MJ device, as well as the volume of semiconductor that is one minority carrier diffusion length away from the depletion regions, is equal to the volume of the depletion region in the SJ device. This analysis ignores the absorption in areas outside of the depletion region.

which will collect it. A large excitation-electrode distance increases the probability that the excited carrier will recombine, losing the energy imparted by the photon.

To remedy this problem, nanowire solar cell geometries were proposed (6). As Figure 6 shows, one variant of a nanowire solar cell is a conductive rod standing axially parallel to the incident light. Each rod is first coated with a doped semiconductor, followed by a semiconductor of the opposite doping. These two semiconductors form a junction surrounding the rod. Finally, a second electrode which is (ideally) transparent to the incident light is deposited onto the geometry.

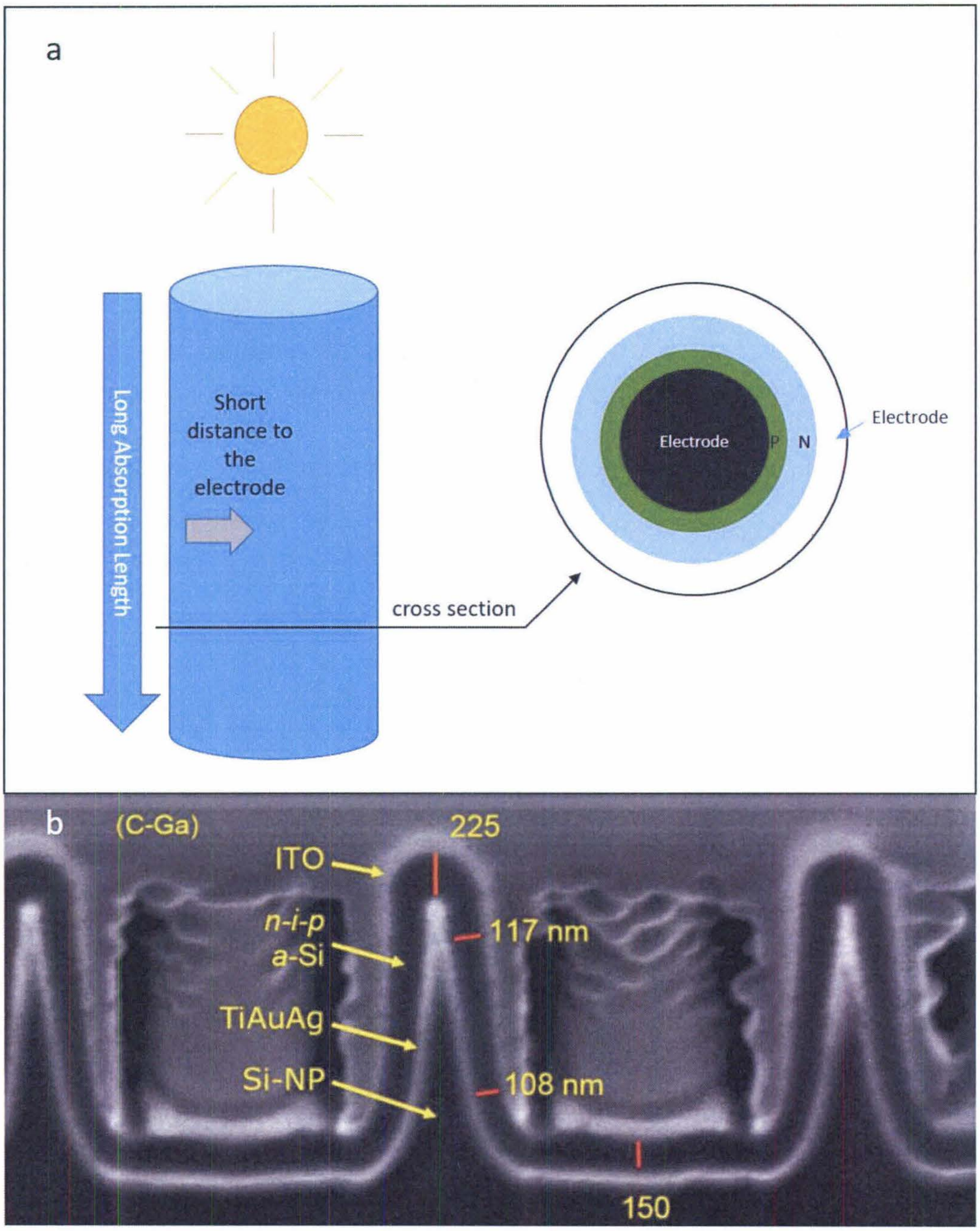

Figure 6 Nanowire Photovoltaic Overview
a) Geometry of a simple nanowire photovoltaic device, and b) electron microscope image of a nanowire solar cell (from (7), used with permission from John Wiley and Sons).

In this configuration, the depletion layer spans the axial length of the rod, L. The length L can be engineered to be substantially longer than a typical layer thickness of a planar depletion region. A crucial note is that the excitation-electrode distance in a nanowire cell is invariant of L, and is approximately the same as that of a planar cell, as will be shown in chapter 6. Accordingly, the path length of light through the depletion region, and likewise the likelihood that light is absorbed, is higher in a nanowire geometry than a conventional planar cell *without increasing the excitation-electrode distance*.

As I have shown, there have been many improvements to the basic single-junction solar cell. This thesis will propose and explore a solar cell geometry that combines these advances.

3 Differential Bandgap Solar Cells: Design and Analysis

3.1 Design Motivation

A silicon single-junction solar cell cannot have an efficiency greater than approximately 30% (8). In order to overcome this limitation, researchers stacked several junctions on top of each other, creating multi-junction solar cells. The theoretical maximum efficiency for a three-junction device is around 67% depending on the assumptions made in the model (9). This efficiency is reached when the bandgaps of the junctions are approximately 1.75 eV, 1.18 eV, and 0.75 eV (4). These bandgaps highly restrict the choice of materials that can be used in these three-junction cells—on top of the already stringent requirements for high-performance solar cell materials including low recombination rates and high absorption properties. The theoretical efficiency gain over a three-junction solar cell for four or more junctions is small, assuming that all of the cells have bandgaps at optimized energies. However, if the bandgaps of the materials in a solar cell with n-junctions aren't equal to the ideal bandgaps for an n-junction cell, which could be the case due to the limited choices of active layer materials, adding more junctions can significantly improve the efficiency, as shown in chapter 4. This thesis demonstrates a method which can be used to create solar cells with many—possibly hundreds or thousands—of junctions stacked on top of each other, reducing the stringent conditions for the materials that can be used in a solar cell which approaches theoretical maximum efficiency.

Further, most solar cells have a tradeoff between the depletion region size and the excitation-electrode distance. On the other hand, the proposed design does not have this tradeoff, nor does it require lattice- or current-matching.

3.2 Design Overview

A differential bandgap solar cell (DBSC) (Figure 7) is composed of several conducting micro- or nano-lattices (Figure 8) stacked on top of each other. Each of these lattices is electrically isolated from every other lattice, while each lattice is connected to a balancing circuit which is connected to an electrical load, such as a lightbulb. Each electrically-isolated lattice serves as an electrode to a solar cell which is deposited onto its beams. The bandgap of each stacked solar cell increases by discreet amounts as the z-dimension of the cell increases.

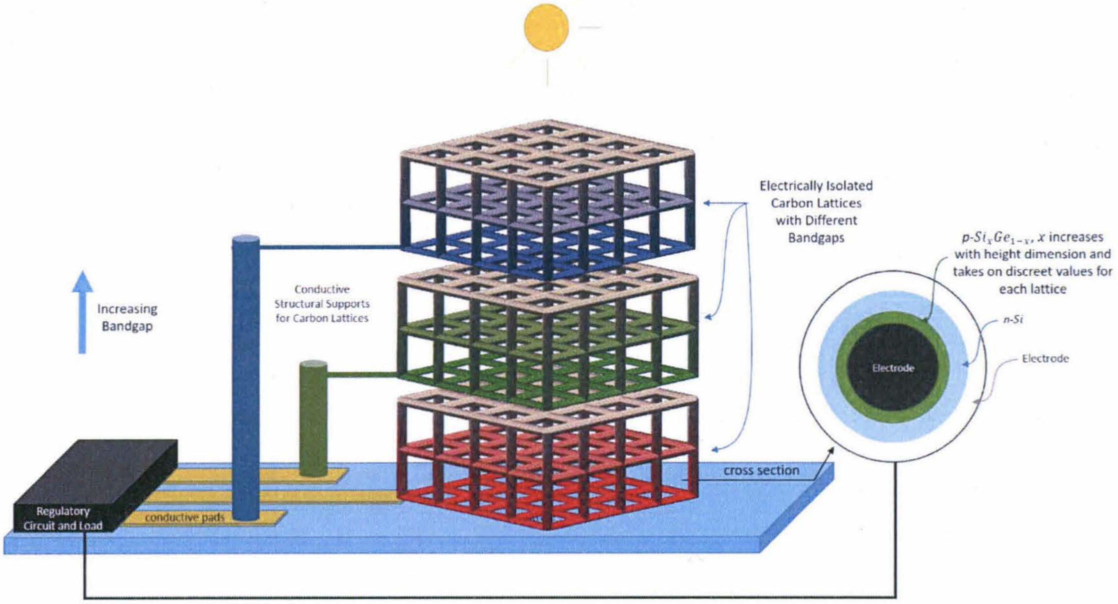

Figure 7: Overview of Main Components of DBSC Device
The active layer is deposited onto three electrically isolated, conducting lattices. Each lattice beam acts as an independent solar cell, creating a multi-junction nanowire design.

3.2.1 Lattice Electrode: Electrically Isolated Stacked Lattices

The lattice electrode is composed of three main parts: 1) a collection of electrically conducting beams organized into unit cells which then form a larger lattice (terminology defined in Figure 8), 2) a conductive pad deposited onto the device's substrate that leads from the lattices to the load and load balancing electronics, and 3) conducting supports which both structurally hold the lattice electrode at a certain height and electrically connect the electrode on the substrate with the suspended lattice. Each independent lattice, after the active layers and the counter electrode (which will be discussed in the subsequent sections) are sputtered, is a photovoltaic device in itself. All of the other portions of the solar cell are deposited onto these electrodes, so the mechanical properties of the solar cell are highly related to those of the lattice electrodes. Likewise, all of the current produced by the photovoltaic travel through these lattices electrodes; it is essential that the electrode material has high electrical conductivity.

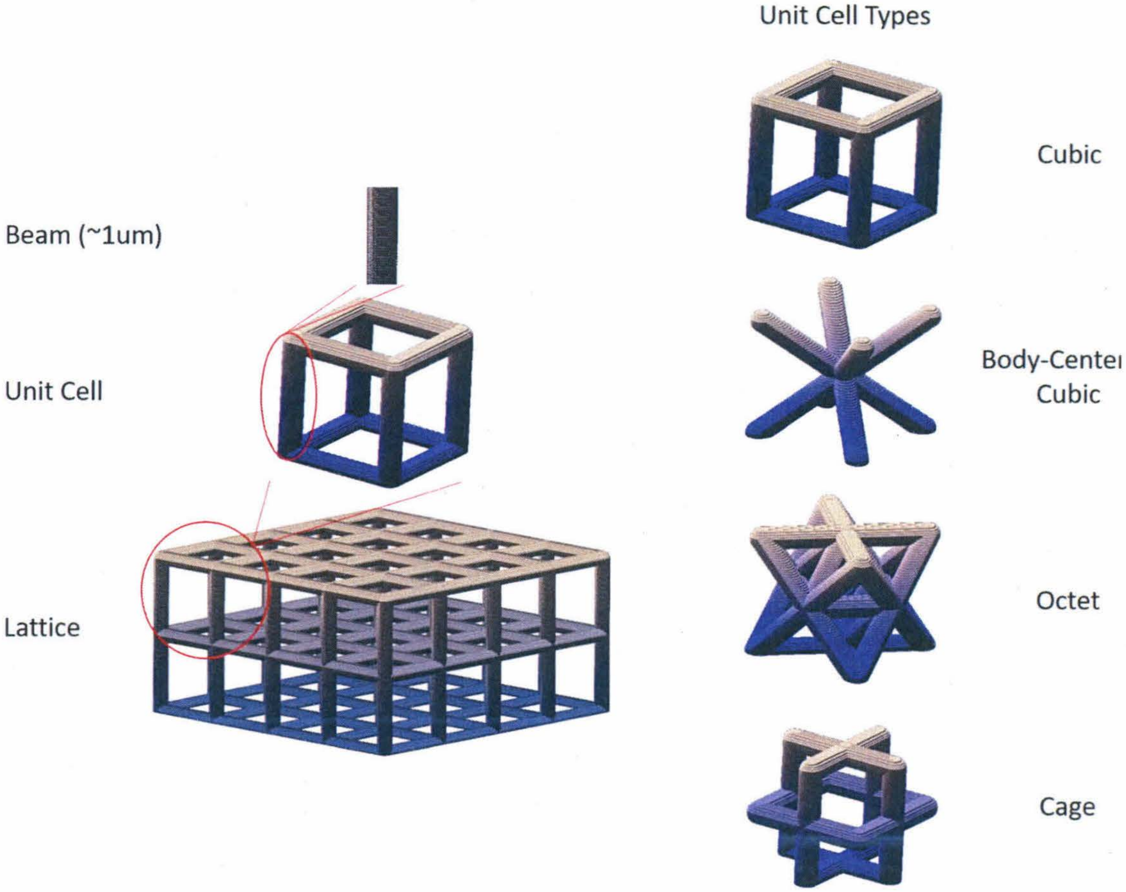

Figure 8: Overview of Structural Components
(Left) Depiction of how a beam composes a unit cell and how the unit cell composes a lattice. These lattices are used as one of the electrodes on a DBSC. (Right) Several examples of possible unit cells which could be used to form DBSC electrode lattices.

3.2.2 Active Layers: Differential Bandgap

The semiconductor materials, called the active layers, are deposited conformally around the lattice electrodes. Two important phenomena occur in these layers: 1) light excites electron-hole pairs (excitons) and 2) the electrons and holes are separated from each other; if this didn't happen, the electrons and holes would likely recombine, dissipating the energy produced by the incident photons. The bandgap of the materials in the active layer dictate the minimum energy for a photon to be absorbed, and once a photon is absorbed the electron has been excited by an amount of energy equal to the bandgap of the material. As discussed above, the bandgap is a parameter that is crucial to optimize in order to increase a photovoltaic's efficiency.

To modify the bandgap of an active layer, a second material with a different bandgap can be added to the material (10) (for example, see Figure 9). According to Vegard's law (11), to first order the bandgap of a material composed of elements A and B, with mole fraction X of element A and $(1 - X)$ of element B can be approximated (12):

$$E_g = XE_{g,A} + (1 - X)E_{g,B} \tag{16}$$

Accordingly, a material that has a bandgap that changes along one dimension, say the z-dimension, can be fabricated by changing the ratio of elements along the z-dimension of the solar cell. *To reiterate, the problem of spatially changing the bandgap of a material is solved by spatially changing the mole-fraction of elements in the material.* There are several methods that could be used to create changing mole-fractions with height; this will be discussed in chapter 6.

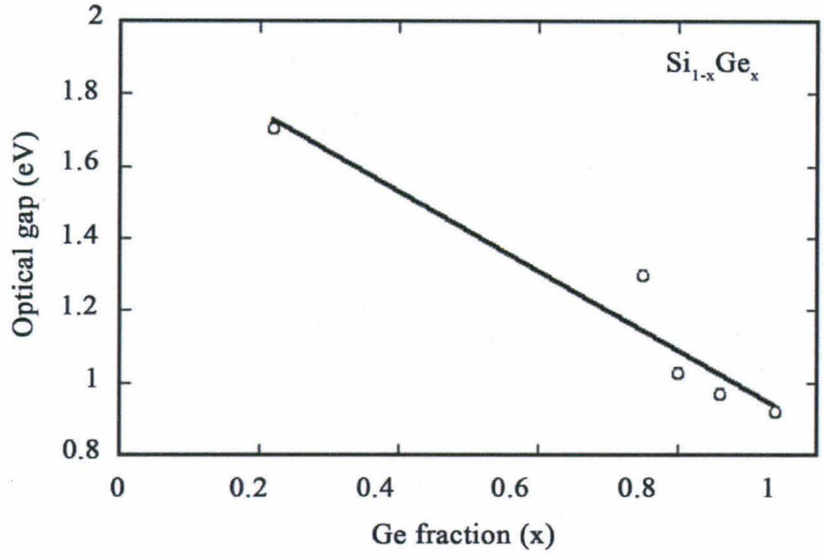

Figure 9: Bandgap of *a*-$Si_{1-x}Ge_x$ as a Function of x
Figure from Pethuraja et al. (13).

This bandgap-altering paradigm can be used with many pairs of elements. Bandgap engineering, however, isn't the only consideration when choosing elements. One of the most important considerations is populations of impurities that trap charge carriers and accelerate their recombination (14). This issue can be mitigated by two strategies: 1) create materials with few impurities or 2) create extremely small active layers so that the excitation-electrode distance is small; even though there may be a certain amount of impurities in the material, the probability of a charge carrier interacting with an impurity while moving to an electrode is low. The second strategy is chosen in this thesis. In a planar solar cell, this method of reducing the absorber layer thickness also reduces the probability of an electron being absorbed by the single active layer. However, in a lattice based solar cell there are active layers on many beams which are stacked on top of each other—so even if a photon passes through the active layer on the first beam, the geometry of the lattice can be designed so that below there are several beams, and likewise several active layers, with the same bandgap. Effectively, the active layer thickness is that deposited on a single beam, multiplied by the number of beams in the lattice. Accordingly, the lattice-based geometry offers a solution that sidesteps the losses in planar solar cells due to the compromise between absorption and recombination probability. Further, a lattice based solar cell has the increased absorption of a nanowire geometry, as discussed above.

Another important consideration for any solar cell is the ease of production: what machines and processes are required to deposit the materials. This logistical consideration ultimately dominated the choice of materials for this thesis. Though there are several pairs of materials with bandgaps that would be sufficient (the ideal bandgaps of the materials will be discussed below), silicon (Si) and Germanium (Ge) were chosen because they are commonly used materials that many laboratories have the infrastructure to deposit.

3.2.3 Outer Electrode

The outer electrode is placed on top of the active layers (see cross section of beams in Figure 7). This electrode needs to provide a conductive path while also allowing light to pass through in order to reach the active layers. The only extra requirement for the outer electrode on a differential bandgap solar cell as opposed to a planar solar cell is that the conductive material should be able to be conformally deposited onto the lattice structures. It is important to note that the active layers deposited onto every lattice electrode will all be connected to the same outer electrode.

3.3 Fabrication Overview

3.3.1 Note on Fabrication

Due to time constraints, the entire fabrication process has not been completed from beginning to end. However, all of the main components of the fabrication process have been tested and are rigorously characterized in chapters 5 and 6.

3.3.2 Fabrication Outline

To make a differential bandgap photovoltaic, the lattice electrodes are first printed onto a Si wafer using two-photon lithography (using a Nanoscribe Photonic Professional GT, Nanoscribe GmbH, Germany). In the two-photon lithography process, a laser is directed through a lens and into photoresist (IP-DIP, a proprietary resin from Nanoscribe GmbH) which is smeared onto the Si wafer. The energy of an individual incident photon (infra-red light) is not enough to crosslink the photoresist monomers. However, near the focal point of the laser, the photon density is high enough that, with a sufficient probability, two photons interact with photoresist monomers simultaneously to polymerize the photoresist monomer (Figure 10). The focal point is moved to create an arbitrary structure programmed and input through the Nanoscribe software within the photoresist.

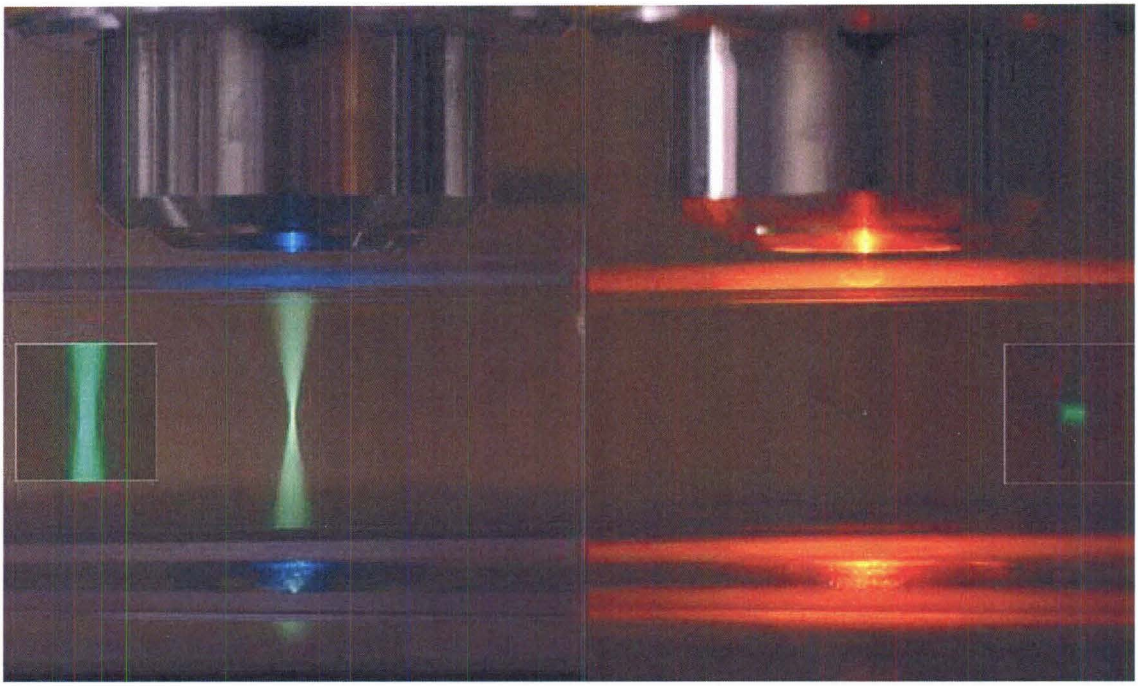

Figure 10: Basics of Two-Photon Lithography
The two images show different wavelength lasers being focused by an objective into a fluorescein solution. On the left, a blue laser has enough energy to excite the solution with a single photon, whereas the infrared laser on the right needs several photons to act in tandem to excite the solution—which is most likely to happen at the focal point. In the same way, during two-photon lithography the laser most likely only has enough energy to crosslink the polymer near the focal point. Image from (15)

Next, the wafer and photoresist is developed, during which all of the non-crosslinked monomers are washed away, leaving the crosslinked photoresist structure. The development process consists of submerging the wafer first for 15 minutes in propylene glycol monomethyl ether acetate (PGMEA), then for 3 minutes in isopropyl alcohol (IPA). To avoid any damage to the structure from the drying IPA, a critical point dryer (Autosamdri-931, Tousimis, Rockville MD) is then used to dry the sample. At this point the sample consists of a photoresist structure attached to the Si wafer through the Van-der-Waals force.

The photoresist structure is then pyrolyzed: the sample is heated in a furnace (Lindberg, Riverside, Michigan) for 5.5 hours at 900°C in vacuum (< 30 mtorr). All elements other than carbon are removed during this process, leaving a carbon lattice that replicates the designed structure with a factor of 4 shrinkage in the dimensions of the edges[10] (Figure 11). This carbon structure is used as the lattice electrode.

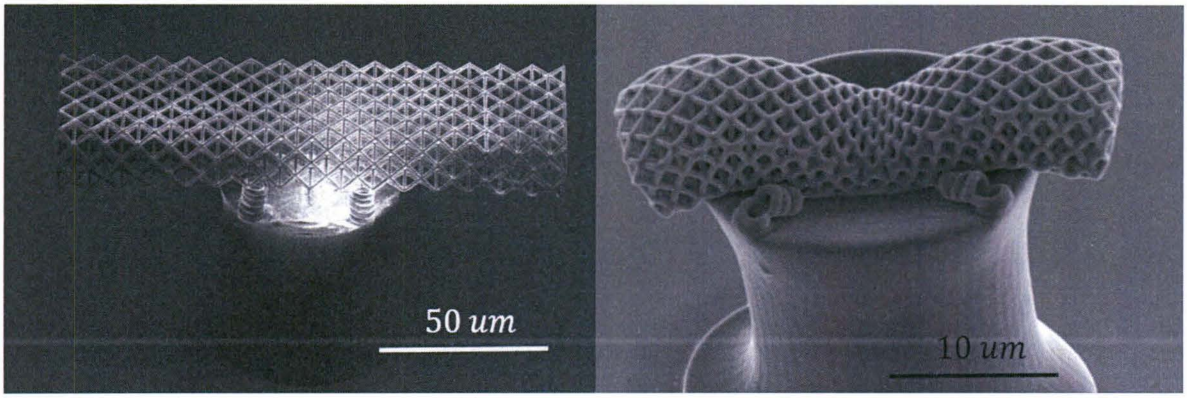

Figure 11: Example of a Lattice Before (Left) and After (Right) Pyrolysis
The structure in the figure is not the lattice electrode but rather a simplified example of the shrinkage during pyrolysis.

Next, the active layers are deposited onto the lattice electrodes using a radio-frequency sputter deposition system (ATC Orion Sputtering System, AJA International, Inc., Scituate, MA) (Figure 12). The material to be sputtered, in a solid form called a "target", is bombarded with ions. This ejects portions of the target towards the device. Conventionally, planar substrates lie with their normal vectors parallel to the ejected material, maximizing the amount of material deposited. Since the lattice geometry limits the mean free path of the ejected particles as they

---

[10] As will be shown in chapter 5, which discusses the pyrolysis process in significantly more detail, the shrinkage isn't uniform and depends on the geometry of the structure being pyrolyzed.

travel towards the substrate, significantly more material is deposited onto the portion of the lattice closest to the target. In this work, however, this phenomenon is rather advantageous for creating a device with a gradient deposition of Si along the height-dimension of the lattice. Gradient material deposition will be explored and characterized in chapter 6.

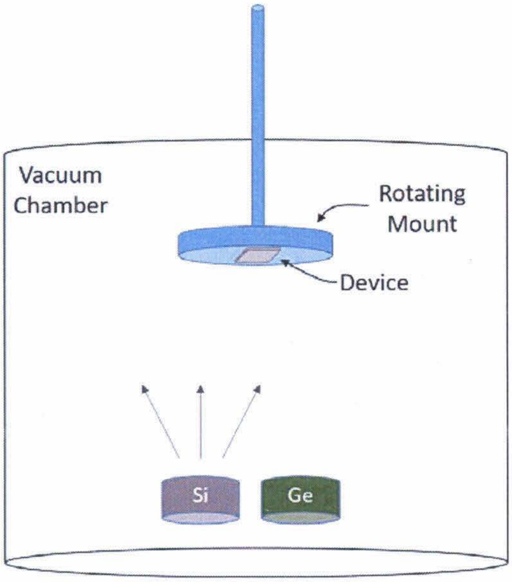

Figure 12: Overview of the Sputter Deposition System
Material is ejected from the targets placed at the bottom of the chamber upwards. Shutters on each target control when the target ejects particulates towards the device. When the shutter is open, particles from the target are shot into the chamber and onto the device, attached upside down on a rotating mount. Some particles which hit the device stick, creating a layer of material.

Before Si is coated onto the device, Ge is first deposited evenly[11] throughout the lattice. To do so, the substrate is mounted onto a 90° device mount—a modified holder for a focused

---

[11] Or atleast significantly more evenly than the Si deposition in the next step.

ion beam (FIB) repurposed to hold a substrate such that the sides of the lattice electrodes are normal to the particles incident from the target (Figure 13). $50\ nm$ of Ge is deposited onto the lattice in four runs, where the substrate is positioned so that in each run a different side of the lattice is placed facing the target.

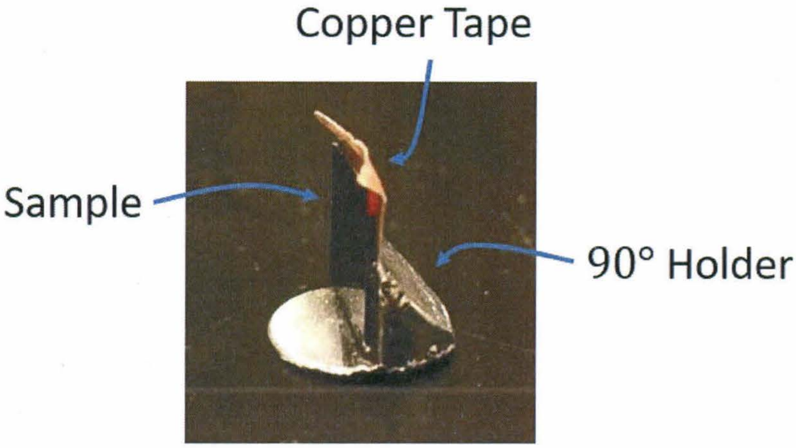

Figure 13: 90° Device Mount For Conformal Sputter Deposition
The flat bottom of the mount is taped to the rotating chuck so that one of the sides of the lattice perpendicular to the substrate is facing the target. Between depositions the sample is rotated with respect to the 90° device mount so that every side of the lattice faces the target for a deposition.

Next, approximately $200\ nm$ of p-doped Si is deposited onto the top beams of the lattice (the layer thickness at the top of the lattice is used as a reference; less Si is deposited throughout the other layers of the lattice during the same deposition, as will be discussed in chapter 6) from only one direction—for this deposition the substrate is positioned with the top face of the substrate and likewise lattice facing the target (as shown in Figure 12). Accordingly, the ratio of Si to Ge is varied with the height dimension of the lattice. The lattice is then annealed for $10\ minutes$ at $900°C$ to mix the Si and Ge layers.

To complete the active layers, approximately 100 nm of n-type Si is conformally sputtered using the same method as the Ge deposition. Finally, 100 nm of indium tin oxide (ITO) is conformally sputtered using the same method as the Ge deposition. The ITO is sputtered from a single target in a mixed argon-oxygen atmosphere.

3.4 New Components and Relation to Previous Work

A DBSC combines several well-studied concepts: the nanowire, multi-junction, and light splitting solar cell geometries, making research from each of these fields highly relevant. I will show in the upcoming paragraphs that the two main differences between these solar cells and a DBSC is the lattice electrode geometry and a spatially-modulated active layer bandgap. Before doing so, it is important to note that the general features of a DBSC—depositing an active layer with a spatially-dependent bandgap on a lattice—can be applied to other types of solar cells and materials. The goal of my project is to prove the concept of a DBSC: I have picked materials, Si and Ge, as well as my fabrication procedure to attain this goal. However, there will be more ideal materials and fabrication procedures, discussed in the conclusion, that are not demonstrated in this thesis.

This demonstration of the feasibility of a Si and Ge based DBSC builds off of previous work analyzing Si and Ge devices, particularly solar cells. A considerable amount of research has been conducted analyzing the electronic properties of Si-Ge alloys (13, 16, 17). Specifically, several studies have refined sputter deposition procedures to create films of both crystalline (18) and amorphous (19) Si-Ge mixtures for solar cell applications. Several studies have examined adding amorphous Si to crystalline Si solar cells because of the high optical absorption coefficient of amorphous Si (20, 21). However, these studies mainly grow crystals on planar surfaces, which provide very different growth environments from the lattice electrodes in a DBSC. It is significantly easier to deposit amorphous material on a DBSC's lattice electrodes: it has been demonstrated by (7, 22-25) that solar cell p-i-n junctions can be made purely from amorphous Si (a-Si). In particular, (7, 22) feature a-Si active layers deposited onto nanoscale cone and rod shaped electrodes, geometries that are extremely similar to the lattice electrodes used in this thesis. Naughton et al.'s (7) nanowire device converted 8% of the incident energy from the sun to output power. A DBSC offers many advantages over these previous designs, including several junctions integrated into one cell and decreased excitation-electrode distances on each rod while still maintaining increased absorption layer volumes due to the many rods in a lattice.

The goal of this study is to prove the plausibility and estimate the efficiency of a well-optimized DBSC solar cell. Previous work (7, 22) has already demonstrated the feasibility of fabricating solar cells on nanowires. To provide a proof of concept of a DBSC, therefore, only requires showing that such nanowires can be made into electrically isolated lattice electrodes (chapter 5), and that active layers with spatially-dependent bandgaps can be deposited onto these lattices (chapter 6).

4 DBSC Simulation

The goal of this section is to compare the energy conversion efficiency[12] of a DBSC to the efficiency of solar cell technology currently available. An important note is that this analysis is meant to be a first pass, proof of concept simulation. The DBSC geometry can be applied to many different materials, and many nuances can be added to a DBSC in order to increase cell efficiency, including back surface fields and light scattering geometries. Accordingly, instead of spending extra time on a specific analysis that is uncharacteristic of DBSC devices at large, this simulation finds realistic, albeit rough estimates for what can be expected of DBSC devices.

To this end, the lattice electrodes will be approximated as planar geometries. This approximation is justified for a DBSC which has a large coverage factor—if a lattice electrode unit cell (defined in Figure 8) with active layers deposited onto it is placed on a substrate and viewed from above, the coverage factor is defined to be the visible surface area of the substrate that is underneath the unit cell (Figure 14). The layer thicknesses in this simulation are $50\ nm$ for the n-type region and $100\ nm$ for the p-type region, taken from (12).

---

[12] Energy conversion efficiency will be referred to as "efficiency" for ease of notation.

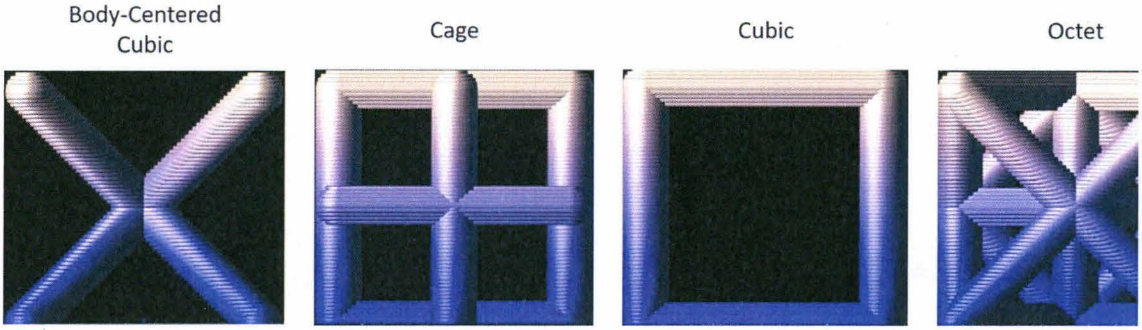

Figure 14: Coverage Factor of Common Unit Cells
The coverage factor of each of these unit cell views is given by the ratio of the surface area of the black and non-black surfaces. The octet has the lowest coverage factor of these unit cells and therefore is the best of these unit cells to be approximated as a plane.

4.1 Solution to Drift and Diffusion Equations

4.1.1 Equations To Be Solved

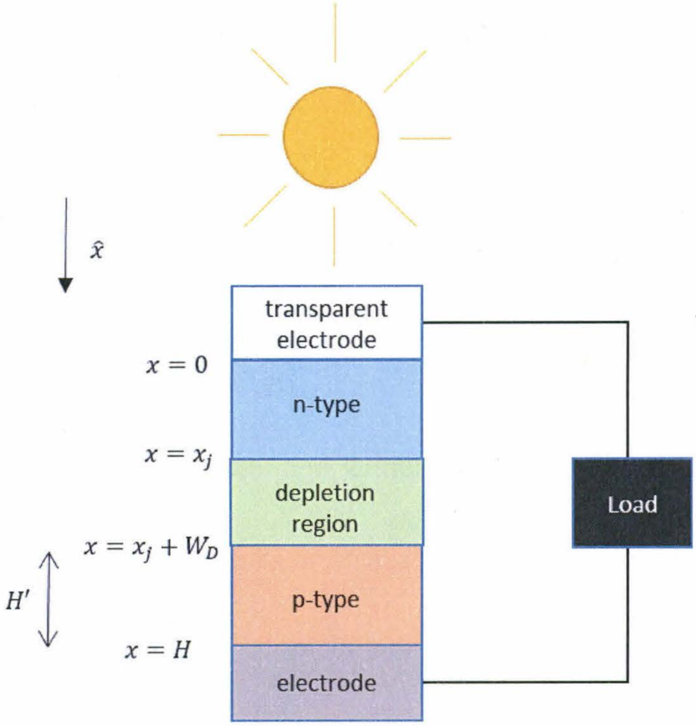

Figure 15: Definition of Geometry for Single Solar Cell Portion of Simulation

Following the analysis of Sze & Ng (26), the electrical properties of a planar solar cell can be modeled by five equations which are presented below. These equations are dependent on ω, the wavelength of incident light, and the geometric parameters defined in Figure 15. This analysis assumes $N_D \gg N_A$, where N_D and N_A are the number of donor and acceptor impurities, respectively. Under this assumption, a majority of the depletion region will be in the p-type semiconductor, allowing the depletion region in the n-type semiconductor to be ignored.

First of all, the light-induced generation rate of electron-hole pairs $G(\omega, x)$ is given by

$$G(\omega, x) = \phi(\omega)[1 - R(\omega)]\alpha(\omega)Exp(-\alpha(\omega)x) \qquad \textbf{17}$$

where $\alpha(\omega)$ is the absorption coefficient, $\phi(\omega)$ is the $\frac{number\ of\ incident\ photons}{time*frequency\ bandwidth}$, and $R(\omega)$ is the reflection coefficient. To better understand equation 17, compare it to the Beer-Lambert law for the intensity of light, I, travelling through a material:

$$I(\omega, x) = I_0 Exp[-\alpha(\omega)x] \qquad \textbf{18}$$

where I_0 is the incident intensity, analogous to $\phi(\omega)[1 - R(\omega)]$ in equation 17. The α dependence in equation 17 can be explained by examining the amount of light which is absorbed in an interval Δx: $\frac{dI}{dx}\Delta x$. Plugging equation 19 into this expression gives $-\alpha(\omega)Exp[-\alpha(\omega)x]\Delta x$, the same form as the α dependence in equation 17.

Next, we know that in equilibrium the number of charge carriers in a region must stay constant, or else an infinite amount of charge could build up. Accordingly, the number of charge carriers that flow out of a region ($\frac{1}{q}\frac{dJ}{dx}$, where J is the carrier current and q is the magnitude of the carrier charge) is equal to the number of carriers that are generated (equation 17) less the number of carriers that recombine in that region (for electrons the amount of recombination is given by $\frac{n_p - n_{p0}}{\tau_n}$ where n_p is the number of electrons in the p-type layer and n_{p0}, τ_n are defined above equation 9; p_n, p_{n0}, and τ_p are similarly defined for holes in the n-type layer):

$$\frac{-1}{q}\frac{dJ_n}{dx} = G_n - \left(\frac{n_p - n_{p0}}{\tau_n}\right) \qquad \textbf{19}$$

$$\frac{1}{q}\frac{dJ_p}{dx} = G_p - \left(\frac{p_n - p_{n0}}{\tau_p}\right) \qquad \textbf{20}$$

where J_n and J_p are the currents of electrons in the n-type layer and holes in the p-type layer, respectively.

The final two equations to be solved relate the current densities to the electric field and gradient in carrier density[13]:

$$J_n = q\mu_n n_p \zeta + qD_n \frac{dn_p}{dx} \qquad \textbf{21}$$

$$J_p = q\mu_p p_n \zeta - qD_p \frac{dp_n}{dx} \qquad \textbf{22}$$

---

[13] Note that while equations 21 and 22 are dependent on ζ which is dependent on the voltage applied across the solar cell, ζ does not impact the solution for the photocurrent—the spatial derivatives of equations 21 and 22, which are independent of ζ, are what affect the photocurrent.

where μ_n, μ_p are the electron and hole mobilities, respectively. ζ is the electric field, and D_n, D_p are the diffusion constants of electrons and holes, respectively.

4.1.2 Solution for a Single Junction Solar Cell

Following (4), the solution to equations 17 - 22 is:

$$J_p = \frac{q\phi(1-R)\alpha L_p}{\alpha^2 L_p^2 - 1} * \left(\frac{\left(\frac{S_p L_p}{D_p} + \alpha L_p\right) - Exp[-\alpha x_j]\left(\frac{S_p L_p}{D_p} Cosh\left[\frac{x_j}{L_p}\right] + Sinh\left[\frac{x_j}{L_p}\right]\right)}{\frac{S_p L_p}{D_p} Sin\left[\frac{x_j}{L_p}\right] + Cosh\left[\frac{x_j}{L_p}\right]} - \alpha L_p Exp[-\alpha x] \right) \tag{23}$$

$$J_n = \frac{q\phi(1-R)\alpha L_n}{\alpha^2 L_n^2 - 1} Exp[-\alpha(x_j + W_D)] * \left(\alpha L_n - \frac{\frac{S_n L_n}{D_n}\left(Cosh\left[\frac{H'}{L_n}\right] - Exp[-\alpha H']\right) + Sinh\left[\frac{H'}{L_n}\right] + \alpha L_n Exp[-\alpha H']}{\frac{S_n L_n}{D_n} Sinh\left[\frac{H'}{L_n}\right] + Cosh\left[\frac{H'}{L_n}\right]} \right) \tag{24}$$

$$J_{dr} = q\phi(1-R) Exp[-\alpha x_j](1 - Exp[-\alpha W_D]) \tag{25}$$

$$J_L(\omega) = J_p(\omega) + J_n(\omega) + J_{dr}(\omega) \tag{26}$$

$$J_{L,Tot} = \int_{\omega_{band\ gap}}^{\infty} J_L(\omega) d\omega \tag{27}$$

where S_p, S_n are the surface recombination velocities on the p- and n- type side, respectively, J_{dr} is the photocurrent density from thermal excitations in the depletion region, and $J_{L,Tot}$ is the total photocurrent density. $J_{L,Tot}$ combines with the generation and recombination currents to produce the total current, given in equation 13. Ultimately, however, this analysis is concerned with the maximum power output of a solar cell; to find this, the current and voltage, I_{max} and V_{max}, that produce this maximum power will be found. Multiplying equation 13 by V to find the cell power output, $P(I,V)$, and then setting $\frac{dP}{dV} = 0$ gives an implicit equation for V_{max} (with $\beta \equiv \frac{q}{kT}$):

$$0 = \frac{dP}{dV} = I_{gen}\left(e^{\beta V_{max}} - 1\right) + I_{gen}\beta V_{max}e^{\beta V_{max}} - I_{L,Tot} \tag{28}$$

$$= I_{max} + I_{gen}\beta V_{max}e^{\beta V_{max}}$$

$$V_{max} = \frac{1}{\beta}\ln\left[\frac{\frac{I_{L,Tot}}{I_{gen}} + 1}{1 + \beta V_m}\right] \approx V_{OC} - \frac{1}{\beta}\ln[1 + \beta V_{max}] \tag{29}$$

$$I_{max} = -I_s\beta V_{max}e^{\beta V_{max}} \tag{30}$$

Accordingly, to solve for the maximum power a given solar cell will produce, first calculate $J_{L,Tot}$ using equation 27. Plug this into and numerically solve equation 29, then multiply the result by equation 30.

4.1.3 Generalizing to Multiple Junctions: Absorption

Each of the lattice electrodes in a DBSC have independent electrical contacts leading out of the solar cell—in other words, each lattice electrode could power a device completely separate from the devices powered by the other lattice electrodes. Accordingly, the power produced by the DBSC is the sum of the power from the individual electrodes. Each of the electrodes can therefore be modeled separately, and their powers can be added—with the caveat that the sun's spectrum is partly absorbed by the upper lattice electrodes before reaching the lower lattice electrodes. As discussed above, each electrode can be modeled as a planar solar cell: therefore, the entire DBSC can be modeled as stacked, planar solar cells.

The spectrum incident on the n^{th} lattice electrode from the top of the device can be calculated by considering the spectrum that is absorbed by the lattice electrodes placed above:

$$\phi_n(\omega) = \phi(\omega)(1 - R)Exp[\sum_{i=1}^{n-1} -\alpha(\omega, x_i)\, H_i]$$

where H_i is defined in Figure 15 and x_i is the fractional amount of Ge in the active layer on lattice electrode i. Note that only one factor of $(1 - R)$ is present: even though light will reflect off of every beam in the cell, any reflections off of lower beams will have to travel through the upper beams before leaving the device, increasing their probability of being absorbed. Due to the geometry of the lattices, the light reflected by a beam will travel in many directions and towards other beams of the cell. For many unit cell geometries that have high coverage factors, there is a large probability that the reflected light will travel through another active layer before leaving the cell. Even though light might reflect off of a particular beam, other diffuse light will be incident on the same beam—so a simple approximation to model this behavior is that the spectrum which travels through each active layer is approximately the same spectrum as is incident on the active layer, ignoring reflections.

It is important to note that the absorption coefficients of Si and Ge are different, and therefore the absorption coefficient of mixtures of $Si_{1-x}Ge_x$ likewise change with x. This is demonstrated in Figure 16. Though this simulation is meant to model amorphous active layers, the only dataset found is for crystalline materials[14]. This data is not ideal[15]: this simulation will not give an accurate value for the theoretical efficiency of an a-Si and a-Ge DBSC. The simulation can still provide significant amounts of information about the relative efficiencies between different solar cell geometries, namely a single-junction solar cell and DBSC's with various parameters.

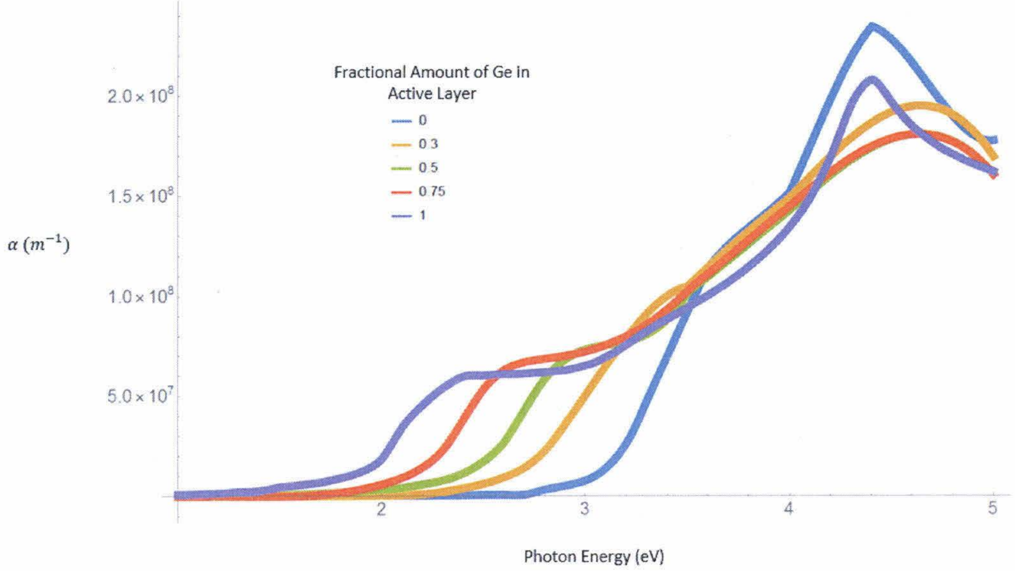

Figure 16: Absorption Coefficient of Active Layers for a Crystalline Alloy
Data from (10).

4.1.4 Absorption Results in a DBSC

An important factor in determining the efficiency of a solar cell is the amount of absorption in the active layers. One of the main benefits of the lattice electrode design is the

---

[14] Several data sets that only measured a small region of energy or an insufficient number of x values were found for amorphous Si-Ge alloys.

[15] The crystalline absorption coefficient deviates at some energies by a factor of approximately 10 from the value for amorphous materials based on the limited amorphous absorption coefficient data that was found. However, at many energies the values differed by approximately a factor of 2.

ability to stack many unit cells on top of each other within each lattice electrode, effectively increasing the volume of the absorption layer without increasing the excitation-electrode distance. This geometry-dependent increase in absorption is shown in Figure 17.

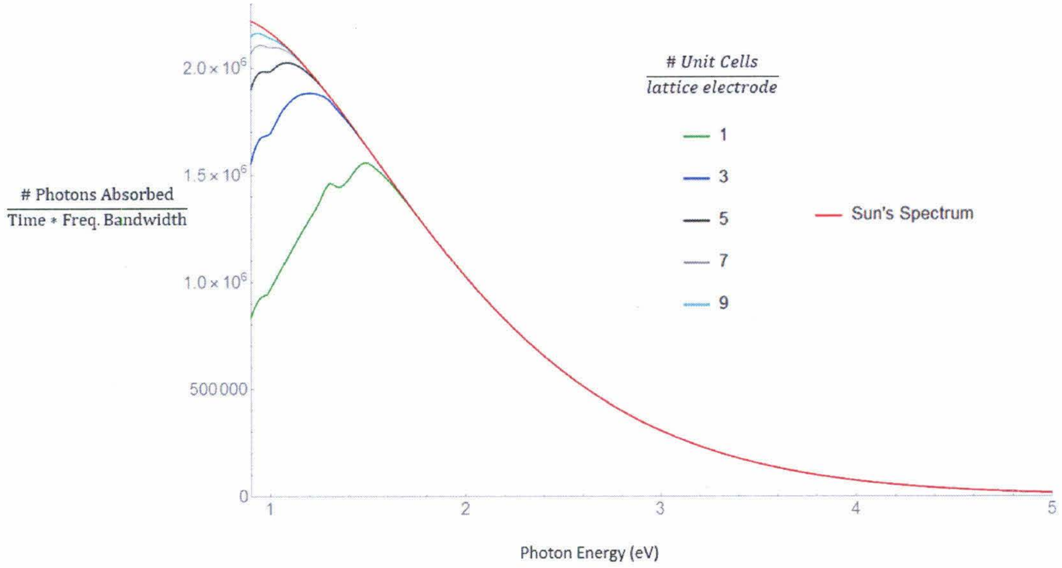

Figure 17: Simulated Absorption Spectrum For Varying Numbers of Unit Cells Per Lattice Electrode
The red line shows the sun's spectrum (assumed to be a perfect black body). The other lines show the number of photons absorbed by a lattice with 10 lattice electrodes stacked on top of each other, where each lattice electrode has the height (in unit cells) given in the legend. These values were calculated by subtracting equation 31 from the sun's spectrum. The active layer widths on each beam is assumed to be 300nm.

4.1.5 Efficiency Results

According to this simulation, the efficiency of a planar a-Si cell (with the same geometry as any of the planes used to approximate the DBSC) is 3.8%, which is consistent with values in (7)[16]. The efficiency for an amorphous, 10 lattice electrode tall DBSC is predicted to be 15.2%: a

---

[16] The efficiency referenced in literature here is 6%, slightly higher than the value found in the simulation. However, this is to be expected because the absorption coefficients for crystalline, not amorphous, Si are used in this analysis.

400% increase in efficiency. Further, if the same 10 lattice electrode tall geometry was coated with a purely a-Si active layer, the efficiency of the solar cell is predicted to be 8.0% efficient. This shows that the geometry and the change in bandgap of the DBSC both significantly contribute to the device's efficiency.

The simulated relationship between the number of stacked lattice sub-cells and the efficiency of a DBSC is shown in Figure 18. The simulation also shows the power produced by each lattice sub-cell, shown in Figure 19. The highest bandgap sub-cell produces the largest power output, which is likely to be for two main reasons: 1) this sub-cell is on the top of the DBSC and therefore has more incident photons than any other cell, and 2) this sub-cell has the highest bandgap, and likewise the largest $V_{open\ circuit}$, so that the least amount of energy is wasted if any given high energy photon excites an electron in this cell. While the incident spectrum and the bandgap decrease for the lower cells, the power output does not simply decrease with decreasing electrode height. This is because there are a large number of photons (as shown in the sun's spectrum in Figure 17) which don't have enough energy to be absorbed by the highest bandgap cells.

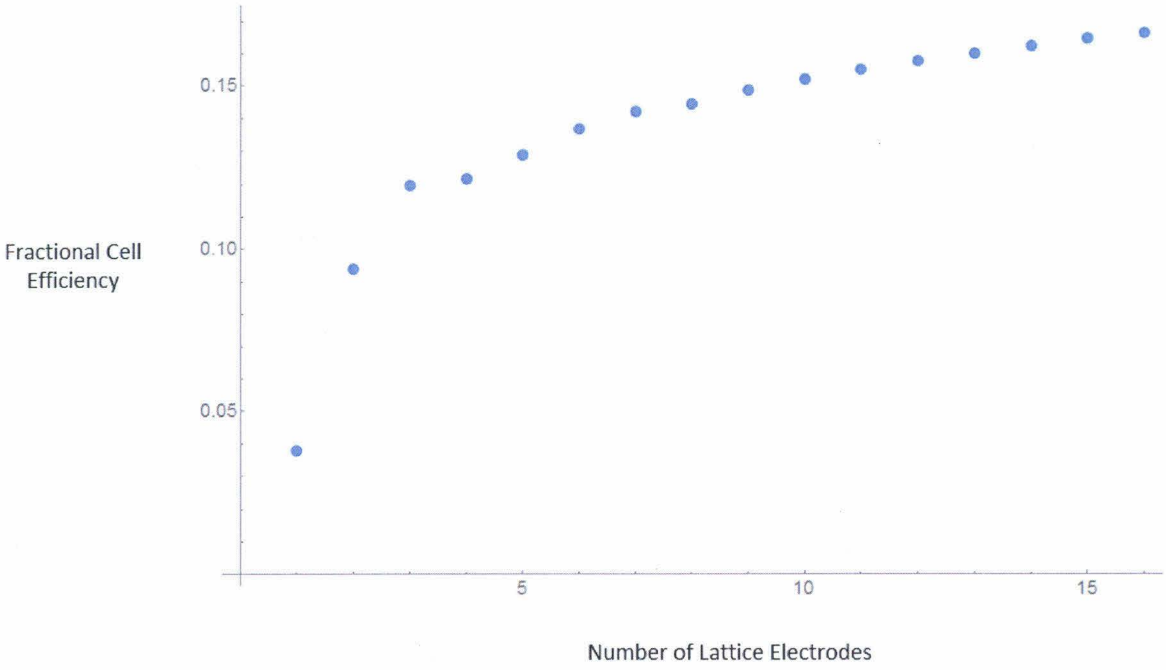

Figure 18: Simulated DBSC Efficiency
An increasing relationship is observed between the cell efficiency (the ratio of the output power to the energy from the sun incident on the cell) and the number of stacked lattices with independent bandgaps in the DBSC. Note that the case of only one lattice electrode is the same as a conventional planar solar cell.

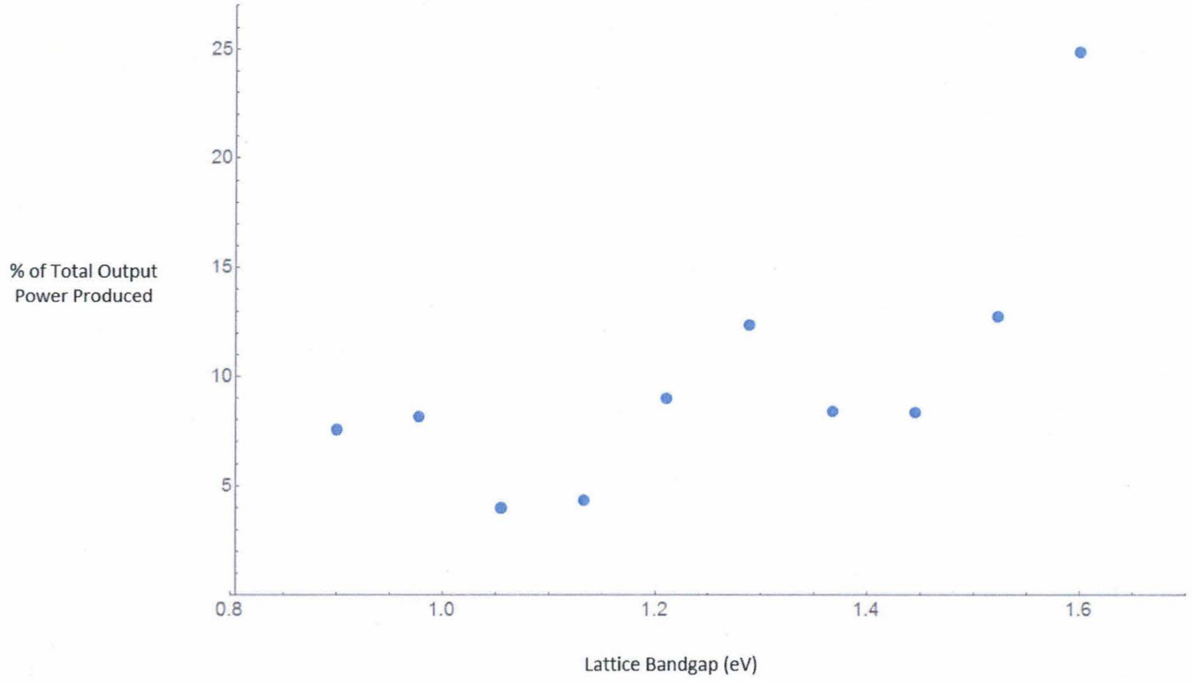

Figure 19: Distribution of Power Produced in Lattice Sub-Cells
Each lattice in a DBSC is electrically isolated from the other lattices, and the power from each of these lattices adds to give the total power, as discussed above. Here, the lattices are labeled by the bandgap of their active layer, which is given on the horizontal axis.

5 Lattice Electrode Fabrication and Analysis

5.1 Lattice Electrode Overview

The lattice electrode has two main functions. First, this electrode must be able to provide the structural support for the rest of the solar cell. All of the other solar cell layers are deposited onto the lattice electrode, and will take whatever shape the lattice electrode takes. Accordingly, the lattice electrode must be able to be fabricated into mechanically robust lattice geometries.

Secondly, the lattice electrode must be able to conduct electrons from the active layers to the load[17]. Both the geometry and the resistivity of the lattice electrode will affect the resistive losses in the paths from the active layers to the load.

To fulfill these functions the lattice electrode has three main components (Figure 20): 1) a lattice structure suspended above other lattices[18] onto which the active layers and counter electrode are deposited, 2) a planar conducting pad connecting to the load, and 3) conductive supports connecting the planar contact to the lattice. Ideally, each of these components is very conductive or slightly conductive and has a high cross-sectional area (as shown in Figure 20) in order to avoid resistive losses.

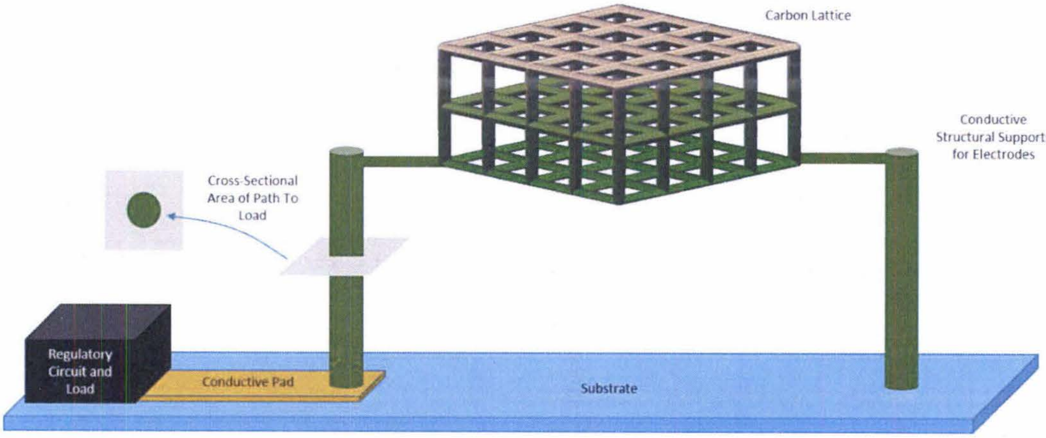

Figure 20: Overview of a Sub-Cell of the Lattice Electrode

---

[17] Or the balancing electronics which then lead to the load. For notational simplicity, this discussion will just use the term "load" to refer to whatever is attached to the lattice electrode, either the load or the load balancing electronics.

[18] Obviously the bottom lattice electrode will not be suspended over other lattices.

One of the potential benefits of creating solar cells out of lattices is the lattices can be used as photonic crystals (27). To this end the lattice parameters could affect how light propagates within the device. For the lattice to work as an optical photonic crystal, the unit cell size of the lattice should be similar to the wavelength of the light, on the order of $500\ nm$. However, this is approximately the side length of the smallest voxel, the volume of the smallest feature size that can be made, with the two-photon lithography process being used[19]. As unit cells are composed of several voxels, the lattices produced directly by the two-photon lithography process used will not function as optical photonic crystals. However, if these lattices are shrunk after being fabricated then the lattice electrode unit cell size should be able to be similar to optical wavelengths.

If the lattices produced by two-photon lithography are heated to several hundred degrees Celsius, they may become conductive (28) and shrink by a factor of approximately 5, as demonstrated below. Therefore lattices produced using two-photon lithography can have small enough unit cells to work as optical photonic crystals while also being conductive. The rest of this chapter will explore this method of fabricating the lattice electrodes.

5.2 Pyrolysis Basics

The lattices produced by two-photon lithography are composed of polymers made from mainly carbon, hydrogen, and oxygen. If these polymers are pyrolyzed then many of the organic

---

[19] The process being used utilizes the Nanoscribe, which claims to be the world's most precise two-photon lithography instrument on its website. Assuming this is the case, the smallest lattices that can be made with two-photon lithography have voxel side lengths on the order of $500\ nm$.

compounds in the polymers will be thermally excited into a gaseous state and leave the lattice (28, 29). During this process, carbon that hasn't left the lattice will begin to form sp^2 bonds, as will be shown below. If pyrolyzed for long enough, most of the oxygen and hydrogen will depart from the structure, leaving carbon. Specifically, the post-pyrolysis structure has been shown (29) to have approximately 5 atoms of oxygen to every 100 atoms of hydrogen. This structure, partly graphitized, is now conductive (29).

5.3 Electrical Characterization of Pyrolyzed Nanostructures

5.3.1 Motivation

While several references exist for the properties of millimeter-long pyrolyzed carbon sheets (for ease of nomenclature, "bulk samples"), no literature was found concerning the electrical properties of polymers forming nano- to few micron- scale structures ("nano-micro structures"). During pyrolysis the organic molecules leave the polymer structure, and the average distance which these exiting molecules must traverse within the structure significantly differs between bulk and nano-micro structures. Accordingly, it is not clear that the material after pyrolysis is the same in these two sizes of structures. Therefore, this section explores the electrical properties of nano-micro structures.

5.3.2 Experimental Setup

To measure the conductivity of pyrolyzed IP-Dip, the proprietary resin created by Nanoscribe GmbH which is used to fabricate the lattice electrode, a 3.44 mm long lattice was fabricated (see Figure 21). The lattice had $n = 6$ and $m = 288$, using the nomenclature defined in Figure 24 (though for the fabricated lattice the longest dimension was horizontal). The lattice dimensions input into the two-photon lithography setup had $12\ um$ long unit cells and a beam radius of $0.75\ um$. Due to the large size of the print, the lattice was written in $n = 6$ and $m = 12$ lattice increments, and these smaller lattices were overlapped by $1.75\ um$ to ensure they wouldn't break apart during pyrolysis. To mitigate the distortion caused by shrinkage during pyrolysis (which will be discussed in detail in section 5.5), the lattice was printed on top of $200\ um$ tall pedestals.

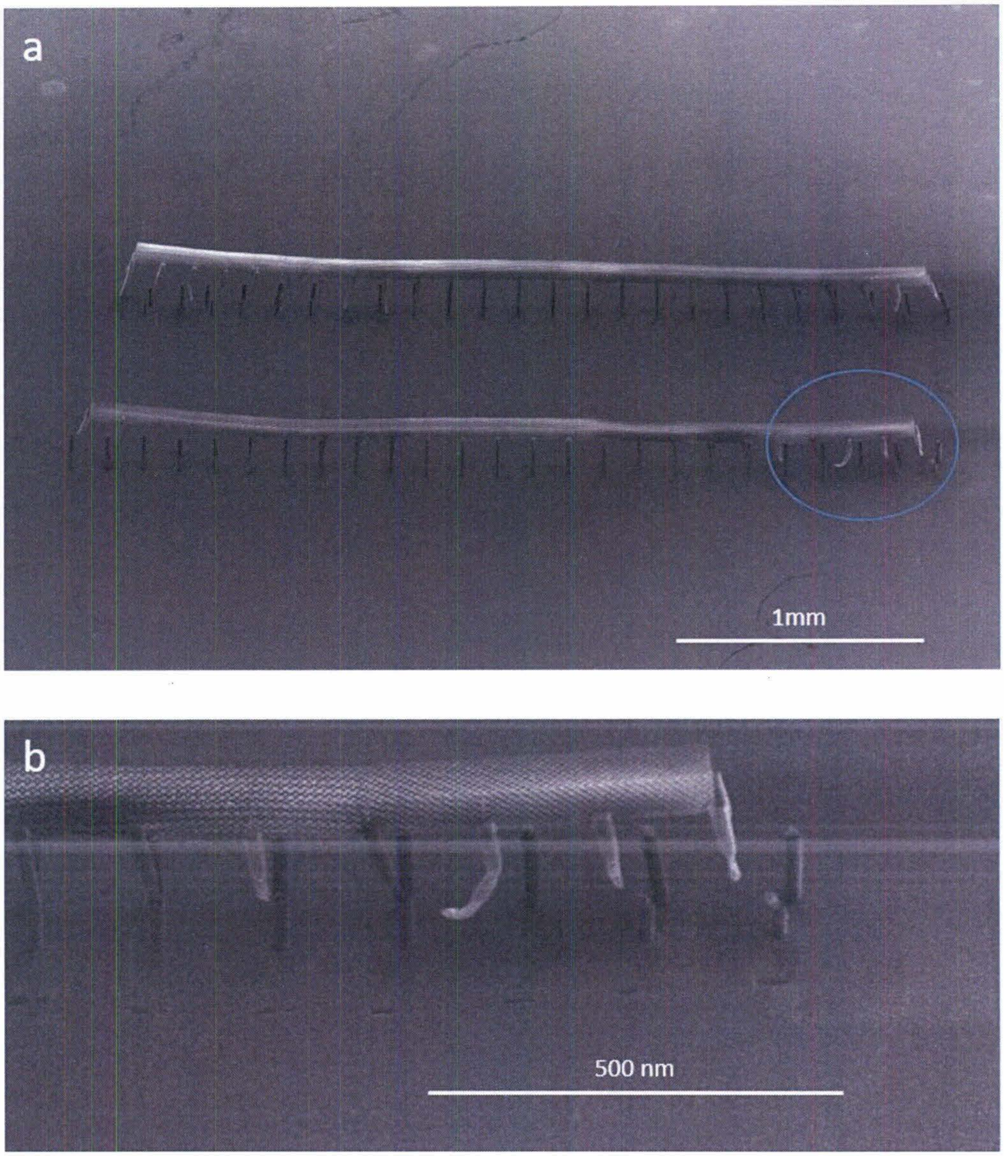

Figure 21: Scanning Electron Microscope (SEM) Image of Lattices For Electrical Conductivity Test Before Being Pyrolyzed
The circle in part (a) covers the region of the lattice which the increased magnification picture (b) shows.

The same post-lithography chemical baths as those described in section 3.3 were used. A focused ion beam (Versa 3D DualBeam, Thermo Fisher Scientific Inc, Waltham, MA) was then used to sever all of the pedestals except for those in the center (shown in Figure 21), which were left to secure the lattice from blowing away in the furnace. With the pedestals on the sides cut, the lattice could shrink without experiencing much tension.

The lattice was then placed in the ceramic oven described in section 3.3 at $900°C$ and $25\ mTorr$ for approximately $6.75\ hours$. Pelco Conductive Silver Paint (Ted Pella, Inc, Redding, CA) was deposited onto either side of the lattice (Figure 22) using a small wire brush and a microscope. The resistivity of the carbon was measured by touching ohmmeter probes to these silver paint electrodes. The resistance across each of the silver paint electrodes was found to be less than an ohm. The pyrolyzed sample geometry was determined using a scanning electron microscope (SEM) (Versa 3D DualBeam, Thermo Fisher Scientific Inc, Waltham, MA).

After the pyrolysis step was carried out, the substrate which held the carbon lattices was found to be slightly conductive. To mitigate this problem, after the resistivity across the silver paste terminals was measured, the carbon lattice was removed with a pair of tweezers. The resistance across the silver paste electrodes was measured again, and this resistance was assumed to be in series with that of the carbon lattices.

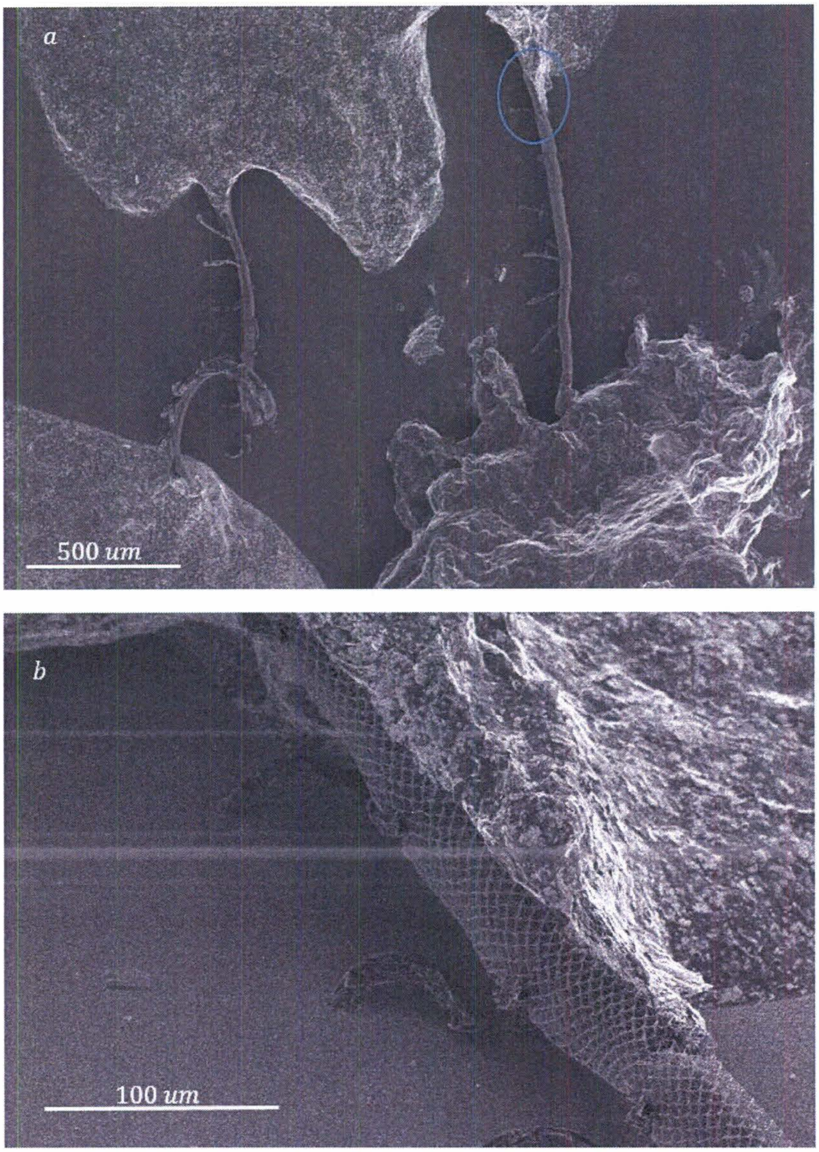

Figure 22: Carbon Lattices With Silver Paint Deposited on Either Edge
The blue circle in (a) gives the region in which (b) was taken. Note that both lattices in this sample connect to the same silver paint electrodes.

5.3.3 Determining Conductivity from Lattice Resistance Measurements

First, consider the resistance of an octet unit cell. Specifically, if the red and yellow planes in Figure 23a are conducting, what is the resistance between them? By symmetry, all of the points in the green plane must be at the same potential, and likewise for all of the beams that run parallel to the green plane. The equivalent circuit between the red and green plane is 12 resistors in parallel, one for each of the beams running between the planes. Accordingly, the equivalent circuit for this unit cell is given in Figure 23b, and the value of the resistance between the red and yellow planes, R_{uc}, is

$$R_{uc} = 2\left(\frac{12}{\rho\frac{l}{A}}\right)^{-1} = \frac{\rho l}{6A}$$

32

where ρ is the resistivity of the beams, A is the cross-sectional area of the beams, and l is the length of each beam running between any two nearest neighbor planes in Figure 23a. Extending this to an $n\ x\ n\ x\ m$ octet lattice (see Figure 24 for an example of a cubic $n\ x\ n\ x\ m$ lattice), the resistance of the lattice, R_{lat}, is

$$R_{lat} = m\left(\frac{n^2}{R_{uc}}\right)^{-1} = \frac{m}{n^2}\frac{\rho l}{6A}$$

33

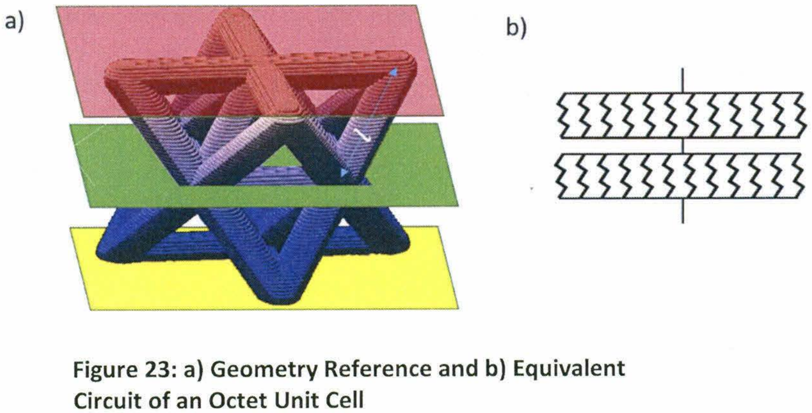

Figure 23: a) Geometry Reference and b) Equivalent Circuit of an Octet Unit Cell

All of the resistance values in (b) are the same, $\frac{\rho l}{A}$.

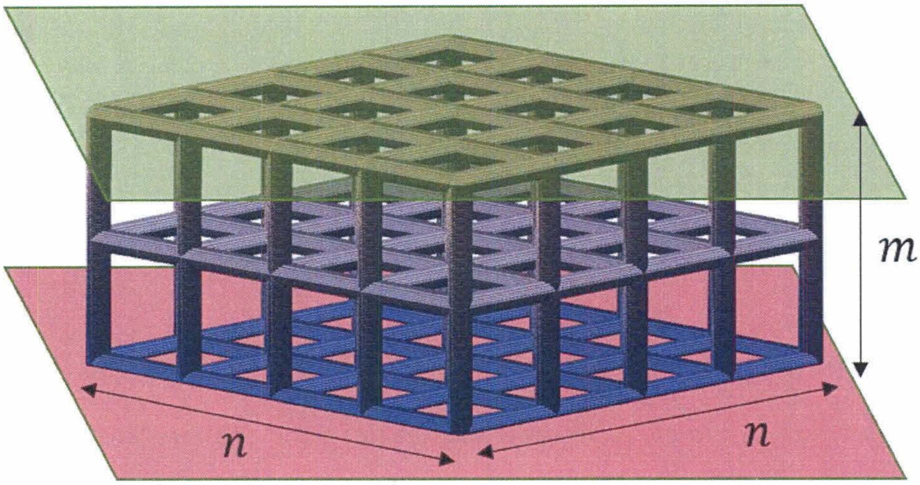

Figure 24: $n\ x\ \ n\ x\ m$ Cubic Lattice
There are n unit cells on each edge of the horizontal plane and m unit cells along the vertical plane.

5.3.4 Results

The resistance across the silver paste electrodes with the lattice intact was found to be $181 \pm 1\ \Omega$. Once the lattice was removed with tweezers, the resistance was $249 \pm 1\ \Omega$. This gives a resistivity of $1.7 * 10^{-4} \pm 5 * 10^{-5}\ \Omega\mathrm{m}$, which is similar to the resistivity of ITO (30), a material commonly used in solar cell electrodes.

5.4 Pyrolyzed Electrode Material Characterization

Raman spectroscopy was used to determine the extent of sp^2 hybridization in the lattice electrode. The number of sp^2 hybridized orbitals is important because the π bonds associated with these orbitals increase the conductivity of the polymer. There are several categories of carbon, including 1) amorphous: highly disordered, 2) glassy: sp^2 bonding regions exist, though don't permeate through all of the sample, and 3) graphitic carbon: the carbon forms graphitic planes, filled with sp^2 hybridized orbitals.

The lattices used in section 5.3 were examined using a Raman spectroscopy setup (custom setup built by and located in the laboratory of Professor George Rossman, California Institute of Technology, Pasadena, CA). The data is given in Figure 25. The relative area underneath the D and G peaks, as labeled in Figure 25, gives information about the sp^2 hybridization in the sample. Let the ratio of the area underneath the G peak to the area underneath the D peak be called the figure of merit, or FOM. An increase in the FOM correlates with an increase in the density of sp^2 bonds in the sample (31, 32). Upon visual inspection, the FOM in Figure 25 is much higher than that in the Raman spectrum of glassy carbon given in (32). According to the metrics used in (32), pyrolyzed IP-Dip polymer is glassy carbon. However, transmission electron microscope results which will be presented in (33) suggest that pyrolyzed IP-Dip is highly amorphous, with several small regions of graphitization.

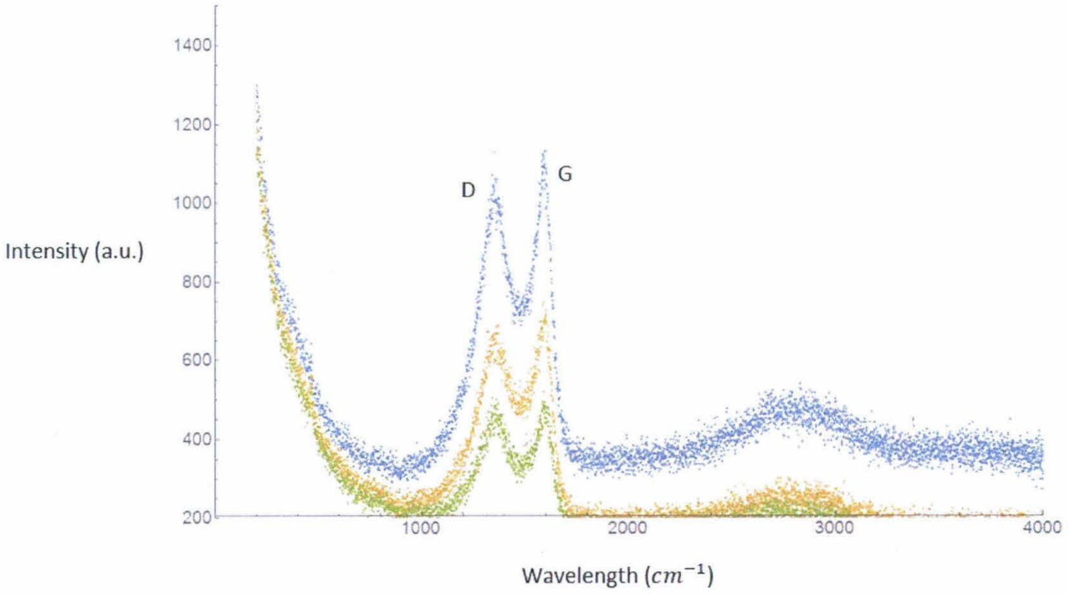

Figure 25: Raman Spectrum of Pyrolyzed Polymer
Each set of datapoints of the same color give the results of a measurement at a single position along the lattice. Different positions along the lattice give different peaks is likely because the laser is not necessarily moved an integer number of unit cells and thus the laser is focused on different parts of unit cells in the lattice, and likewise after pyrolysis the lattice isn't completely uniform (see Figure 22).

5.5 Geometric Pyrolysis Effects: Electrode Lattice Fabrication

The lattice electrode must function as a structural support for the active layers and counter electrode. To ensure that pyrolyzed polymer can form a robust lattice electrode, a proof of concept lattice electrode was fabricated. Researchers have taken rudimentary steps towards creating structural geometries that behave in desired manners under pyrolysis (34). For example, to mitigate the stress on a nanolattice as it shrinks, nanolattices are put on top of cylindrical pedestals that also shrink (as shown in the top right image of Figure 26). Lattices are also mounted on springs for the same reason.

Creating a lattice electrode composed of electrically isolated stacked lattices adds several degrees of complexity to the design process. First, the suspended lattices need supports, and the supports should be conductive to create an electrical pathway from the active layers to the pads which lead to the load. A solution which was undertaken in this thesis is to print the supports out of polymer as well—in which case the supports shrink during pyrolysis. The design process to create suspended, isolated lattices that can survive pyrolysis is detailed in the rest of this section.

The first step was to determine how far a lattice could overhang off of one of its supports. Several overhanging geometries were fabricated:

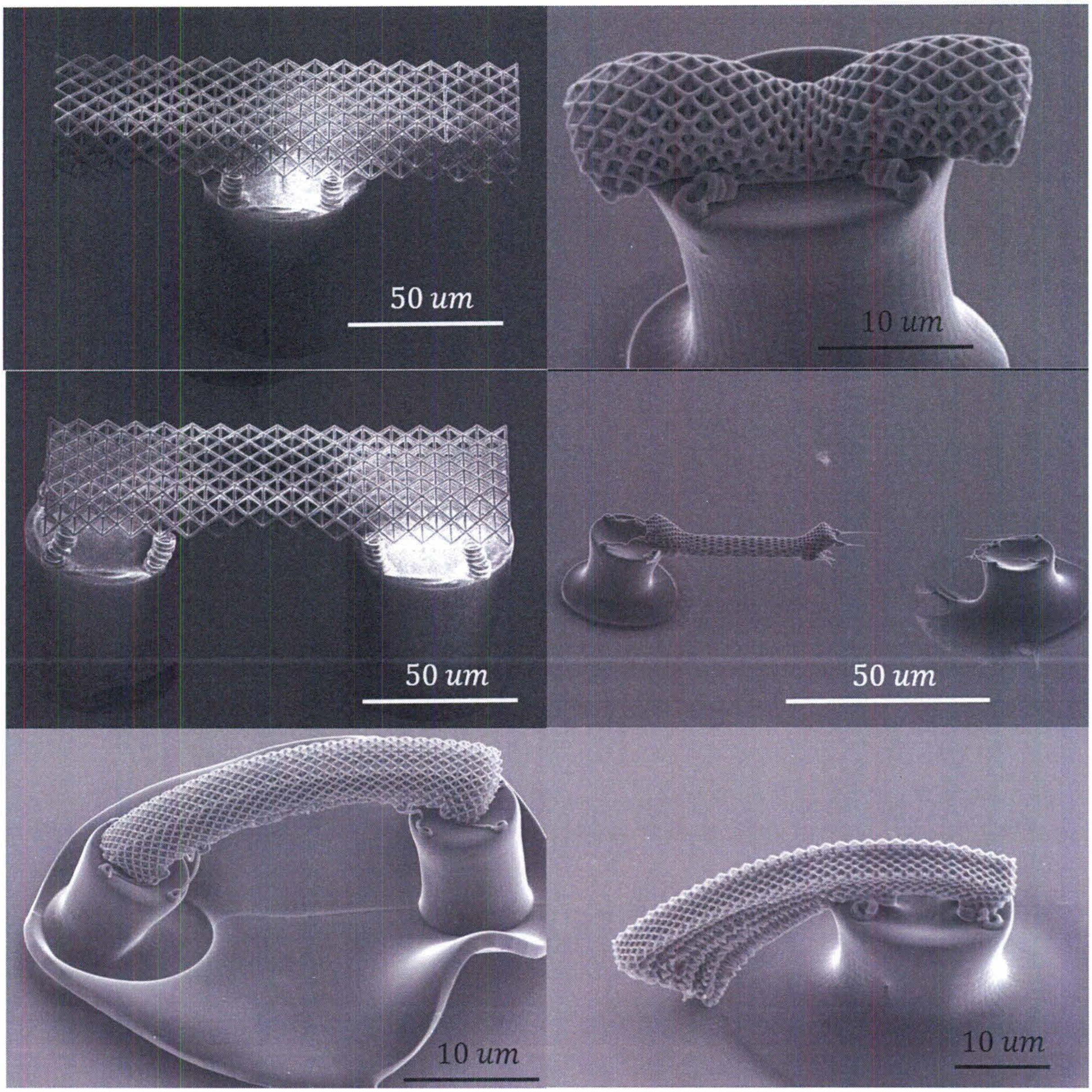

Figure 26: Structures Testing The Effects of Overhanging Geometry During Pyrolysis.
The top two rows demonstrate the unpyrolyzed (left) and corresponding pyrolyzed (right) structures. The middle right picture demonstrates that pyrolyzed lattices can be suspended from a single pedastal. In the bottom row, an attempt was made to make the distance between the pedestals shrink in the same way that the lattice shrinks during pyrolysis. The bottom right photo depicts a sample in which the layers of the lattice weren't properly connected during two-photon lithography because the bottom layers weren't rigidly supported and could move around during the lithography run.

One method of suspending lattices is to support each lattice from the side, as demonstrated below:

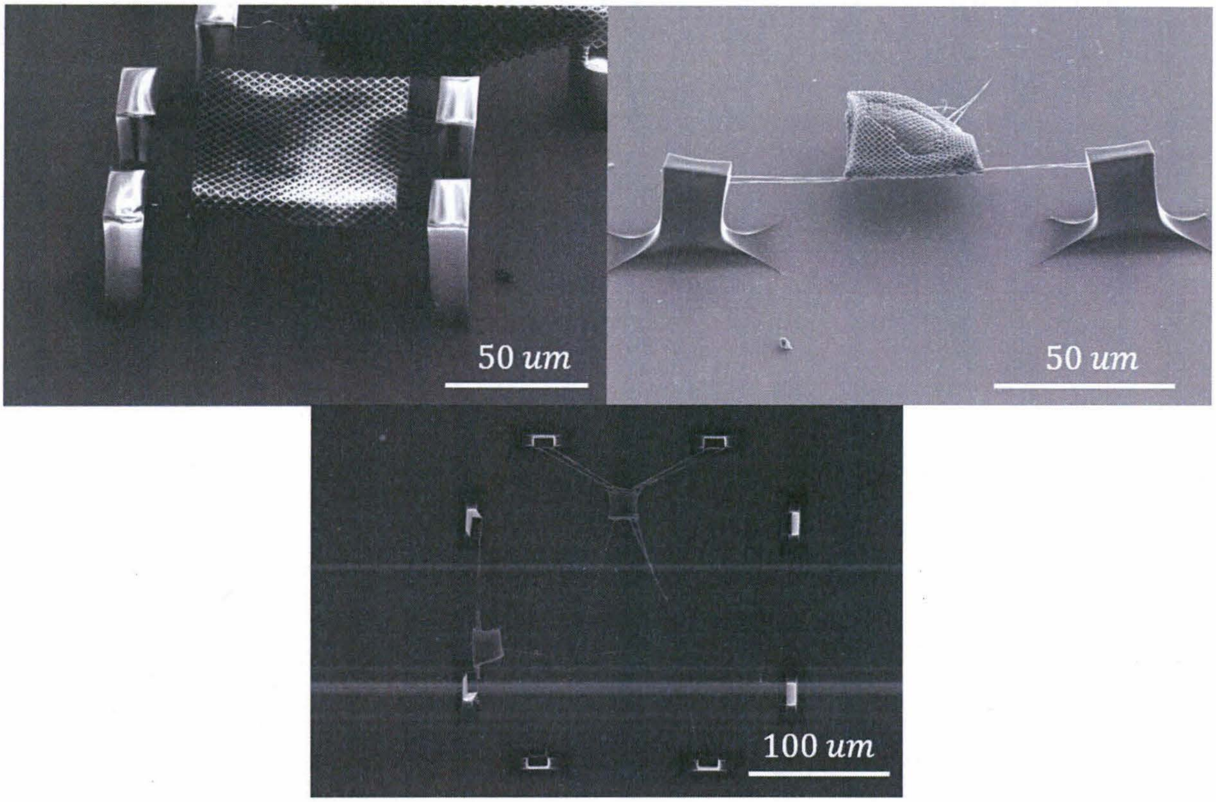

Figure 27: Lattices Suspended by Their Sides
The top right photo is the pyrolyzed version of the top left geometry. The bottom photo demonstrates an attempt to suspend two lattices on top of each other. The unpredictable shrinkage in the springs using this method made aligning the suspended lattices difficult.

The structures that pyrolyzed the most predictably were symmetric structures, so symmetric hollow cylinders were fabricated to suspend lattices on top of each other:

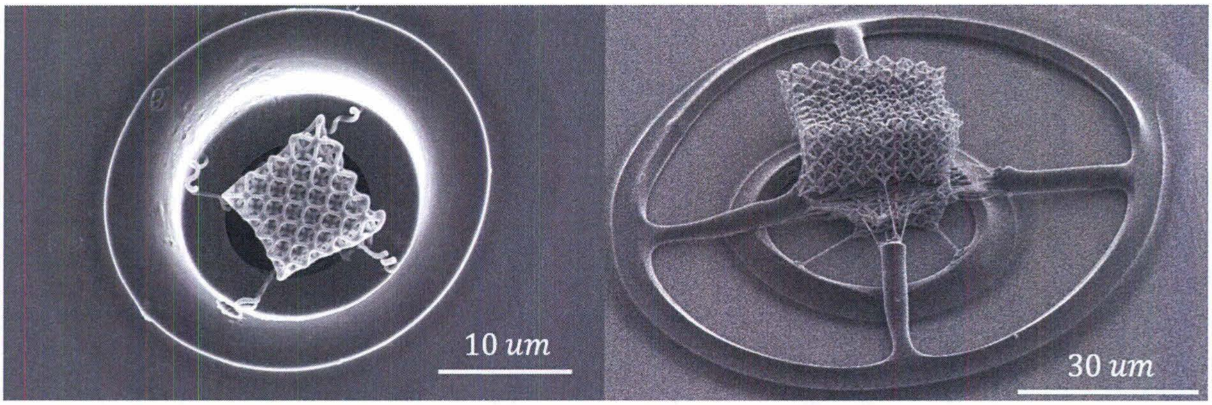

Figure 28: Pyrolyzed Lattices Suspended By Hollow Cylindrical Pedestals
The left photo is a single lattice on a hollow pedestal, while the right photo shows a failed attempt at suspending a top lattice from small pedestals mounted on a larger diameter cylindrical pedestal.

As the lattices shrunk they put a significant amount of tension on the top of the pedestals, causing the pedestals to bend inward (Figure 28). Making the pedestals wider and shorter led to a lattice successfully suspended on top of another:

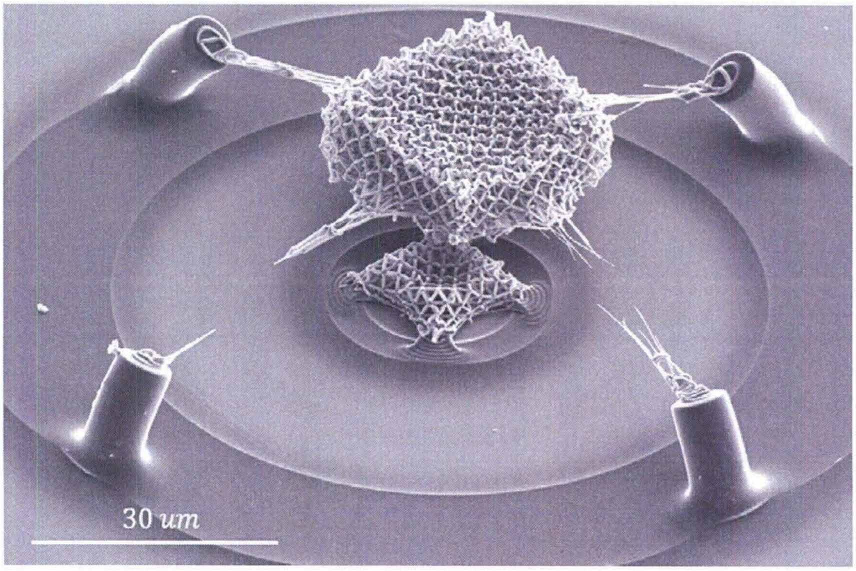

Figure 29: Lattice Successfully Suspended Over a Second Lattice After Pyrolysis

Figure 29 shows the main component of the lattice electrode: the suspended lattices. Conducting pads can be evaporated onto the substrate and then masked such that the two-photon lithography process prints the conducting pedestal of each suspension system on top of exposed contacts that run underneath the other cylinder pedestals and to the load. Though Figure 29 only demonstrates a two lattice electrode, sub-cells with the same geometry as the top lattice in Figure 29, though increased pedestal diameter and height, can be added to create more layers of suspended lattices.

6 Differential Bandgap Active Layer Deposition

6.1 Overview

6.1.1 Motivation

A significant amount of energy is wasted in a single-junction solar cell. As was discussed in chapter 2 and demonstrated computationally in chapter 4, a large portion of the energy in a high-energy photon is wasted because the electron excited by the photon dissipates energy until the excited electron has energy $E_0 + E_g$, where E_0 is the electron's initial energy and E_g is the bandgap of the material. To remedy this problem, multi-junction solar cells were made. A DBSC is similar to a multi-junction cell in that the DBSC has junctions with different bandgaps stacked on top of each other. This chapter discusses how these junctions are fabricated.

6.1.2 Fabrication and Chapter Outline

The height dependence of the bandgap in the Si and Ge based DBSC considered in this thesis is achieved by increasing the amount of p-doped Si deposited on the lattice sub-cells as the height-dimension of the lattices increase (see Figure 30). The amount of Ge deposited onto the lattices stays constant with the height dimension. Accordingly, the ratio of the amount of Si to Ge on the lattices increases with the height of the lattices. This creates a bandgap that increases along the height dimension of the solar cell, as discussed in chapter 2.

Once the Si and Ge are deposited on the lattice electrodes, the active layers are annealed to ensure the Si and Ge are well mixed and the Si-Ge mixture conformally coats the entire lattice electrode. An astute reader may have noticed that the active layer formed by the Si-Ge mixture will vary in thickness with the height-dimension of the lattice. This will cause variations in the excitation-electrode distance, which will change the likelihood of electrons recombining with holes before the charge carriers get to the electrodes. The excitation-electrode distance therefore can't be optimized throughout the entire lattice, which is a drawback of the current fabrication method. However, other fabrication methods which overcome this problem are outlined in the conclusion section.

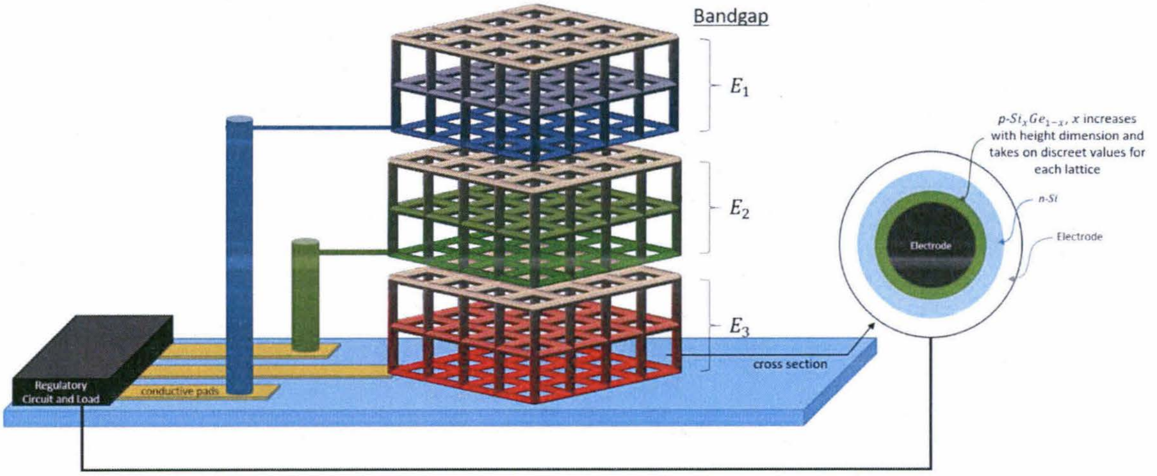

Figure 30: Bandgaps of Sub-Cells in a DBSC
If the DBSC has n electrodes, then $E_1 > E_2 > \cdots > E_n$. Note that the entire lattice in a sub-cell has approximately the same bandgap.

There are several main components of the deposition process. First, Ge (and later the n-type Si, deposited after annealing the Si-Ge mixture, and the outer electrode, deposited after the n-type Si) is deposited conformally. This conformal deposition is explored in section 6.2. The p-type Si needs to be deposited in a height dependent manner—this will be explored in section 6.3. Finally, the Si-Ge layer is annealed, which will be discussed in section 6.4.

6.2 Conformal Deposition[20]

Using the conformal sputtering apparatus and procedure described in section 3.3, $50\ nm$ of Ge was deposited onto each side of a pyrolyzed rotated body-centered-cubic lattice with a unit cell size of $4\ um$. The lattices were then imaged with an SEM (instrument referenced above) (Figure 31). The Ge was clearly distinguishable from the carbon, allowing for the Ge layer depth to be easily measured. The depths of Ge in several stacked unit cells was measured, yielding an average layer depth of $49\ nm$ with a $5\ nm$ standard deviation, showing the conformity of the deposition process.

---

[20] The sputtering of the lattice was done by Ryan Ng and the imaging was done by Victoria Chernow, both working under Professor Julia Greer at the California Institute of Technology, Pasadena, CA. The data is used with their permission.

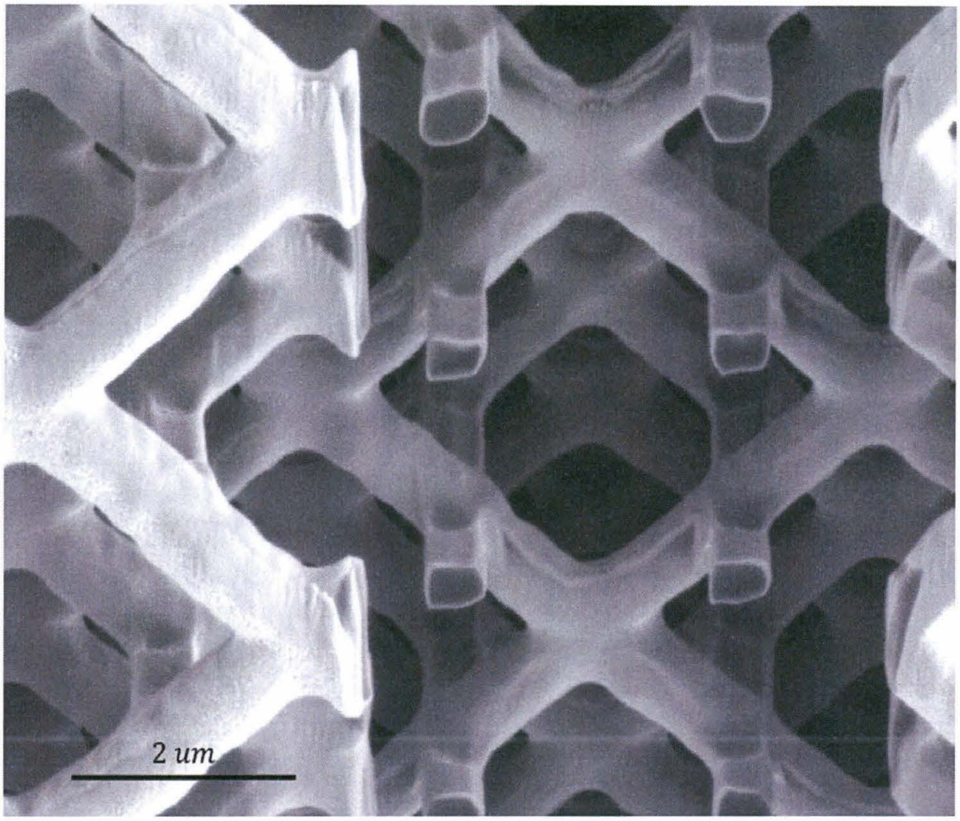

Figure 31: Conformal Ge Deposition
The dark area in the middle of each beam is carbon, while the light shell is Ge.
Figure courtesy Victoria Chernow.

6.3 Spatially-Dependent Semiconductor Deposition

6.3.1 Experimental Setup

Each sample was composed of 9 lattices: for three different unit cells (body-centered cubic, octet, and cubic, all of which are shown in Figure 8) three lattices of different unit cell sizes were fabricated. The unit cell sizes that were input into the two-photon lithography setup (the setup and post-lithography development process are the same as those explained in section 3.3) were $20\ um$, $25\ um$, and $30\ um$. The dimensions of the different sized lattices, in terms of unit cells, was 7x7x7, 5x5x5, and 3x3x3, respectively[21]. The samples were heated to $900°C$ for approximately $5.5\ hours$. Finally, silicon was deposited onto the samples with the sputtering system (described in section 3.3) for approximately $8\ hours$. In order to obtain a change in the amount of Si deposited along the height of the lattice, the lattice was positioned such that the top of the lattice (the face parallel to but furthest from the substrate) was placed facing the targets from which the Si was ejected.

To measure the amount of Si deposited on each beam, the diameters of the lattice beams as a function of the beams' height dimension along the lattice was measured. The thickness of the beams was found using an SEM (the same instrument cited in section 6.2).

---

[21] The dimensions of the lattices were constrained to a $140um$ x $140um$ box in the x and y dimensions. Making the lattices larger than this box would have increased the two-photon lithography time significantly or damaged the structural integrity of the lattices, especially after pyrolysis.

6.3.2 Results

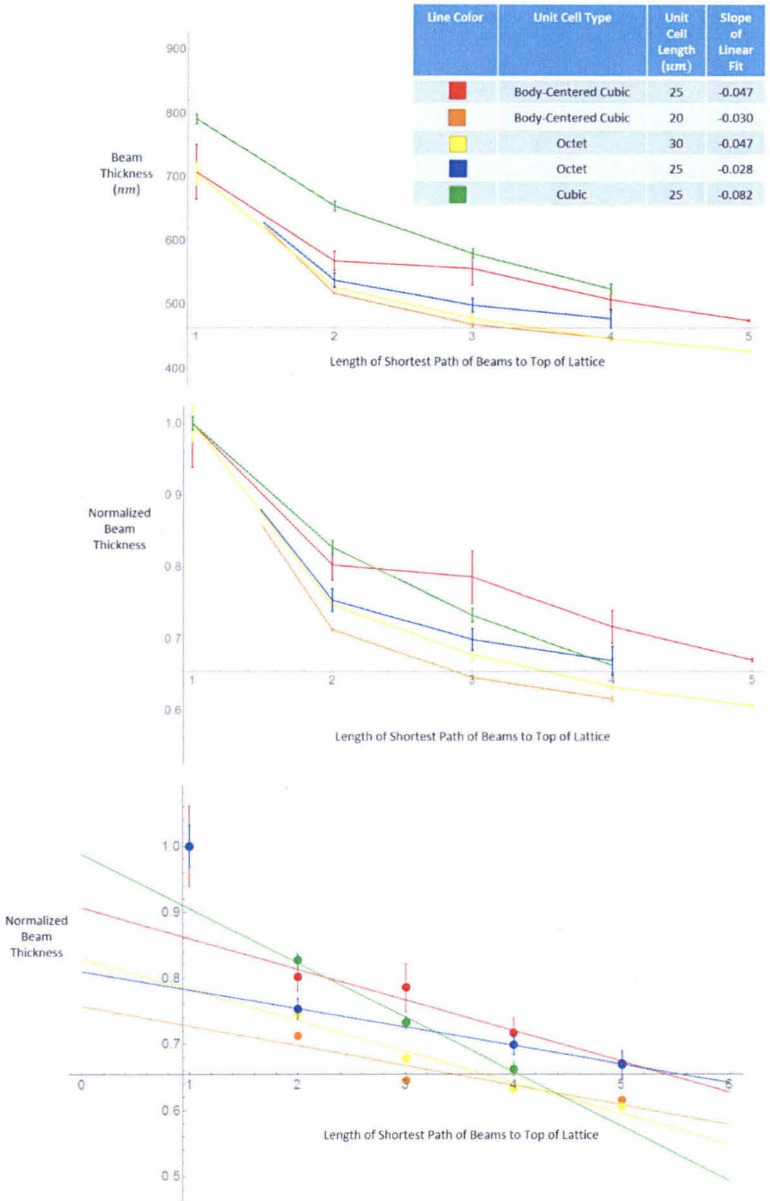

Line Color	Unit Cell Type	Unit Cell Length (um)	Slope of Linear Fit
🟥	Body-Centered Cubic	25	-0.047
🟧	Body-Centered Cubic	20	-0.030
🟨	Octet	30	-0.047
🟦	Octet	25	-0.028
🟩	Cubic	25	-0.082

Figure 32: Height Variation in Beam Thicknesses Due to Si Sputtering on Nanolattices

The unit cell length given in the table denotes the lattice parameters input into the two-photon lithography system. The horizontal axis is the shortest number of beams traversed to reach the top of the lattice. In the middle plot, the set of beam thicknesses for each lattice was normalized by the average of the top unit cell's beam thicknesses. Linear fits are displayed in the bottom plot for each lattice, excluding the top beam of the lattice.

The results are given in Figure 32. The beam thickness, variations in which are caused by the change in the depth of Si sputtered onto the beams, decreases as the height dimension decreases. Linear and exponential fits were attempted on the data though resulted in significant residuals.

There are two main portions of data in Figure 32: the beams in the top unit cell and all of the other beams. A significant drop in beam thickness occurs between these two regions because the beams in the top unit cell don't have any structures obstructing their line of sight to the target which is depositing material, significantly increasing the flux of particles onto these beams. The behavior of the beams other than those at the top follow approximately linear lines, as shown in Figure 32 (residuals omitted for brevity). The slopes increase in magnitude for increases in unit cell lengths—which is intuitively clear because the height difference between consecutive measurements is greater for a larger unit cell. To make general claims about the regression slopes of different lattice geometries and unit cell sizes, more data needs to be taken. However, the main goal of this section—to prove that a semiconductor can be deposited onto a lattice with decreasing amounts of deposition as the height dimension of the lattice decreases—has been completed.

6.4 Annealing Si-Ge Layers

This section will demonstrate the plausibility of mixing Si and Ge through annealing, as well as determine the parameters for the annealing process on Si and Ge based DBSC's with the active layer heights given in chapter 4. First of all, the coefficient of diffusion, D, of a material along a one-dimensional path parameterized by x, is defined as

$$\frac{dC}{dt} = D\frac{d^2C}{dx^2} \tag{34}$$

where C is the concentration of the material in question and t is the time. The solution to equation 34 is

$$C(x,t) = \frac{\eta}{\sqrt{t}}e^{-\frac{x^2}{4Dt}} \tag{35}$$

where η is a constant which depends on the initial conditions. In the case of depositing Si on top of Ge, let C represent the concentration of Si in the Ge layer. Let x give the distance perpendicular to the Si-Ge interface into the Ge layer. Applying the boundary condition that the total number of Si atoms, N, is constant gives (as done in (35))

$$N = \int_0^\infty C(x,t)\,dx = \eta\int_0^\infty e^{-\frac{x^2}{4Dt}}\,d\left(\frac{x}{\sqrt{t}}\right) \tag{36}$$

$$= 2\eta\sqrt{D}\int_0^\infty e^{-\left(\frac{x}{\sqrt{4Dt}}\right)^2}\,d\left(\frac{x}{\sqrt{4Dt}}\right)$$

$$= \eta\sqrt{\pi D}$$

resulting in $\eta = \frac{N}{\sqrt{\pi D}}$. Therefore

$$C(x,t) = \frac{N}{\sqrt{\pi Dt}}e^{-\frac{x^2}{4Dt}} \tag{37}$$

Equation 37 models a singular region of extremely high concentration spreading out—which isn't the case for the DBSC. However, a characteristic timescale for the diffusion process can be gained from 37. A measure of the extent of how much a substance has diffused is given by the turning point of equation 37, which occurs at

$$x_{turn}(t) = \sqrt{2Dt} \tag{38}$$

To model the initial conditions of Si diffusing into Ge, the initial state of a Si layer lying on top of a Ge layer can be approximated as $C(x, t_0)$, the spread of the singular region of concentration (the region at $t = 0$ in equation 37) after a time t_0, where $x_{turn}(t_0) = l_s$ with l_s being the depth of the Si layer. As shown in Figure 33, in this approximation some of the Si starts in the top layers of the Ge. This aids the validity of the argument, because the Si molecules being deposited have enough kinetic energy to *ballistically mix* with the already-deposited Ge (36). The time it takes for the Si to diffuse approximately evenly throughout the Ge is given by $t_{end} - t_0$, where $x_{turn}(t_{end}) = l_{active\ layer}$ with $l_{active\ layer}$ being the combined height of the Si and Ge layers. Accordingly, the approximate diffusion time to mix the layers is given by

$$t_{end} - t_0 = \frac{1}{2\mathrm{D}}(l_{active\ layer}^2 - l_s^2) \tag{39}$$

For the active layer parameters used in chapter 4 and an annealing process at $900°C$, at which temperature Si has a coefficient of diffusion in Ge of approximately $2.1 * 10^{-13}\,\frac{cm^2}{s}$ (37)[22], the annealing time is approximately $476\ s$.

---

[22] This data is for Si diffusing into crystalline Ge because of the lack of values for amorphous Ge in literature. However, Ge may begin to crystallize at the proposed annealing temperature of $900°C$ according to 38. Blum N & Feldman C (1975) The Crystallization of Amorphous Germanium Films. *The Journal of Non-Crystalline Solids* 22:29-35.

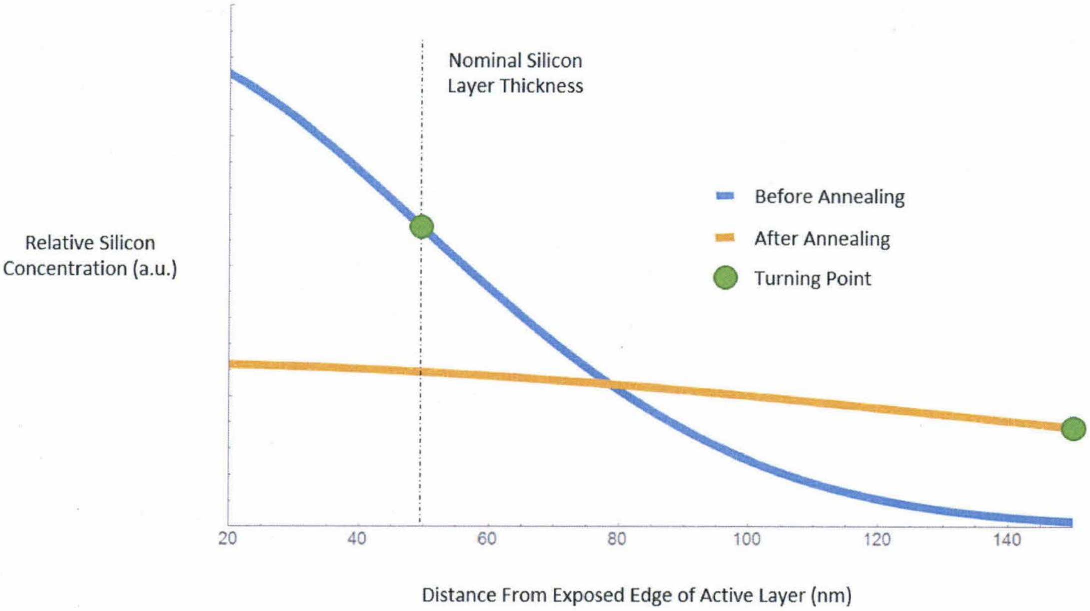

Figure 33: Demonstration of Characteristic Length of Diffusion Paradigm
The pre-annealing line is given by equation 37 with $t = \frac{l_S^2}{2D}$ such that the turning point of the concentration lies at $50\ nm$, the average thickness of the Si layer. Likewise, the post-annealing line is given by equation 37 with $t = \frac{l_{active\ layer}^2}{2D}$ such that the turning point lies at the total active layer thickness.

During this annealing process, carbon could diffuse into the Si Ge mixture. However, the diffusion coefficient of carbon in Si is approximately 2 orders of magnitude lower than that of Si in Ge[23] (39). Therefore, the carbon diffusion during annealing is significantly less than that of Si.

Another consideration is the surface diffusion of the active layer: if there is any inhomogeneity in the layer thickness on any beam due to the sputter deposition process, the annealing process could help smooth the surface out. The surface diffusion of Si on itself is half

---

[23] The coefficient of diffusion of carbon in Ge hasn't been measured, to the author's knowledge. However, if the coefficient of diffusion of carbon in Ge became a problem, then the Si layer could be deposited onto the lattice first followed by the Ge layer, so that the carbon would be in contact with Si more than Ge through the annealing process.

that of Si diffusing into Ge (40). On the other hand, the gradient of the layer thicknesses isn't nearly as severe as the abrupt Si concentration gradient at the start of the Ge layer, so the resulting surface diffusion during the annealing time given above will only be able to significantly smooth out defects that are smaller than the length Si diffuses into the Ge layer.

7 Conclusion

First, this thesis showed computationally that an amorphous Si-Ge DBSC can increase power conversion efficiency by a factor of 4 compared to planar amorphous crystalline solar cells. The same simulation was used to predict the efficiency gains as more sub-cells are added to a DBSC.

Next, it was demonstrated that a DBSC lattice electrode can be fabricated out of conductive amorphous/glassy carbon. The conductivity of this carbon was found to be close to that of ITO, which is conventionally used for transparent electrodes.

Finally, the ability to deposit active layers with both constant and height-dependent layer thicknesses was demonstrated. The framework for determining a geometry-dependent deposition characterization was created, though more data should be taken before conclusions are drawn.

Chapters 4 and 5 prove that the two biggest challenges in converting a planar solar cell to a DBSC, fabricating the lattice electrode and depositing the active layers, can be surmounted. Accordingly, this thesis serves as a proof-of-concept for a new class of solar cells, DBSC devices.

The materials and fabrication procedures considered in this thesis are not necessarily ideal for a DBSC. First of all, the sputter deposition method used only allows for a gradient of either Si or Ge, leading to uneven active layer thicknesses throughout the lattice. This problem could be fixed by removing the DBSC substrate and sputtering (or depositing in another fashion) material from either side. Amorphous Si and Ge were chosen for ease of fabrication rather than for achieving higher power output. Materials with a bandgap wider than that of Si can potentially harness high-energy photons more efficiently. Likewise crystalline materials epitaxially grown on the lattice could reduce the recombination rate.

In order to meet the main goal of this thesis, to significantly increase our ability to produce sustainable energy, the possibility of mass-manufacturing a DBSC should be considered. While many aspects of the DBSC fabrication process can easily be scaled to the industrial level, including sputtering the active layers, fabricating the lattice electrode at a large scale is currently a considerably harder issue. Several methods are being developed for lattice architecture at the nano- and micro- scale (34, 41), though these processes are in their infancy and need to be further developed before they can be used to manufacture lattice electrodes for practical DBSC devices.

A DBSC has many similarities to currently studied solar cells; many of the advances made for other photovoltaics can be applied to DBSC devices. For example, new materials developed with high absorption coefficients can be sputtered onto a lattice electrode instead of the Si and Ge active layers used in this thesis. Further, the low excitation-electrode distance, high active layer volume, and ability to fabricate a large number of independent, stacked junctions afforded by a DBSC opens the door to many, potentially revolutionary, materials which would otherwise be unable to be incorporated into solar cell technology.

Works Cited

1. Lewis NS (2007) Toward Cost-Effective Solar Energy Use. *Science* 315(9 February 2007):798 - 801.
2. Administration USEI (2016) Electric Power Monthly with Data for December 2015. (U.S. Department of Energy).
3. Ashcroft & Mermin (1976) *Solid State Physics* (Holt, Rinehart and Winston, Philadelphia).
4. Sze SM & Ng KK (2007) *Physics of Semiconductor Devices* (John Wiley & Sons, Inc., New Jersey).
5. Henry CH (1980) Limiting efficiencies of ideal single and multiple energy gap terrestrial solar cells. *Journal of Applied Physics* 51(8):4494-4500.
6. Kayes BM, Atwater HA, & Lewis NS (2005) Comparison of the device physics principles of planar and radial p-n junction nanorod solar cells. *Journal of Applied Physics* 97(11):114302.
7. Naughton MJ*, et al.* (2010) Efficient nanocoax-based solar cells. *physica status solidi (RRL) - Rapid Research Letters* 4(7):181-183.
8. Shockley W & Queisser HJ (1961) Detailed Balance Limit of Efficiency of p-n Junction Solar Cells. *Journal of Applied Physics* 32(3):510-519.
9. Kurtz S, Myers D, McMahon WE, Geisz J, & Steiner M (2008) A comparison of theoretical efficiencies of multi-junction concentrator solar cells. *Progress in Photovoltaics: Research and Applications* 16(6):537-546.
10. Kasper E ed (1995) *Properties of Strained and Relazed Silicon Germanium* (Short Run Press Ltd., Exeter, England).
11. Denton AR & Ashcroft NW (1991) Vegard's law. *Physical Review A* 43(6):3161-3164.
12. Singh AK, Tiwari J, Yadav A, & Jha RK (2014) Analysis of Si/SiGe Heterostructure Solar Cell. *Journal of Energy* 2014:1-7.
13. Pethuraja GG*, et al.* (2012) Effect of Ge Incorporation on Bandgap and Photosensitivity of Amorphous SiGe Thin Films. *Materials Sciences and Applications* 03(02):67-71.
14. Nelson J (2007) *The Physics of Solar Cells* (Imperial College Press, London, England).
15. Ruzin S & Aaron H (
16. Eisele C*, et al.* (2003) Laser-crystallized microcrystalline SiGe alloys for thin film solar cells. *Thin Solid Films* 427(1-2):176-180.
17. Kube R*, et al.* (2010) Composition dependence of Si and Ge diffusion in relaxed Si1−xGex alloys. *Journal of Applied Physics* 107(7):073520.
18. W Yeh, M Matsumoto, & Sugihara K (2015) Fast and Low-temperature sputtering epitaxy of Si and Ge and its application to

optoelectronics. in *2015 International Symposium on Next-Generation Electronics* (IEEE, Taipei).

19. Serenyi M, Betko J, Nemcsics Á, Khanh NQ, & Morvic M (2003) Fabrication of a-SiGe structure by rf sputtering

for solar cell purposes *phys. stat. sol. (c)* 0.

20. Tanaka M*, et al.* (1992) Development of New a-Si/c-Si Heterojunction Solar Cells: ACJ-HIT (Artificially Constructed

Junction-Heterojunction with Intrinsic Thin-Layer). *Jpn. J. Appl. Phys* 31:3518-3522.

21. Jagannathan B & Anderson WA (1996) Properties of Sputtered Amorphous Silicon/Crystalline Silicon Solar Cells. in *PVSC* (IEEE, Washington DC).

22. Kuang Y, van der Werf KHM, Houweling ZS, & Schropp REI (2011) Nanorod solar cell with an ultrathin a-Si:H absorber layer. *Applied Physics Letters* 98(11):113111.
23. Carlson DE & Wronski CR (1976) Amorphous silicon solar cell. *Applied Physics Letters* 28(11):671-673.
24. Banerjee A & Guha S (1991) Study of back reflectors for amorphous silicon alloy solar cell application. *Journal of Applied Physics* 69(2):1030-1035.
25. Hsu C-M*, et al.* (2012) High-Efficiency Amorphous Silicon Solar Cell on a Periodic Nanocone Back Reflector. *Advanced Energy Materials* 2(6):628-633.
26. Anonymous (!!! INVALID CITATION !!! {}).
27. Chernow VF, Alaeian H, Dionne JA, & Greer JR (2015) Polymer lattices as mechanically tunable 3-dimensional photonic crystals operating in the infrared. *Applied Physics Letters* 107(10):101905.
28. Singh A, Jayaram J, Madou M, & Akbar S (2002) Pyrolysis of Negative Photoresists to Fabricate Carbon Structures for Microelectromechanical Systems and Electrochemical Applications. *Journal of The Electrochemical Society* 149(3):E78.
29. Ranganathan S, McCreery R, Majji SM, & Madoua M (2000) Photoresist-Derived Carbon for Microelectromechanical Systems and

Electrochemical Applications. *Journal of The Electrochemical Society* 147(1):277-282.
30. Li Q*, et al.* (2015) Defects evolution and their impacts on conductivity of indium tin oxide thin films upon thermal treatment. *Journal of Applied Physics* 118(2):025304.
31. Ferrari AC & Basko DM (2013) Raman spectroscopy as a versatile tool for studying the properties of graphene. *Nature nanotechnology* 8(4):235-246.
32. Wang Y, Alsmeyer D, & McCreery R (1990) Raman Spectroscopy of Carbon Materials: Structural Basis

of Observed Spectra. *Chem. Mater.* (2):557-563.
33. Kudo A & Greer J (2017).
34. Bauer J, Schroer A, Schwaiger R, & Kraft O (2016) Approaching theoretical strength in glassy carbon nanolattices. *Nature materials* 15(4):438-443.
35. Zang L (Lecture.
36. Csik A*, et al.* (2001) Interdiffusion in amorphous Si/Ge multilayers by Auger depth profiling technique. *Journal of Applied Physics* 89(1):804-806.
37. Silvestry H, Bracht H, Larsen AN, Hansen JL, & Haller EE (2006) Diffusion of silicon in crystalline germanium

Semiconductor Science and Technology 21(6).
38. Blum N & Feldman C (1975) The Crystallization of Amorphous Germanium Films. *The Journal of Non-Crystalline Solids* 22:29-35.
39. Kalejs JP, Ladd LA, & Gösele U (1984) Self-interstitial enhanced carbon diffusion in silicon. *Applied Physics Letters* 45(3):268-269.
40. Acosta-Alba PE, Kononchuk O, Gourdel C, & Claverie A (2014) Surface self-diffusion of silicon during high temperature annealing. *Journal of Applied Physics* 115(13):134903.
41. Zheng X*, et al.* (2014) Ultralight, ultrastiff mechanical metamaterials. *Science* 344(6190):1373.